Global Biogeochemical Cycles®

RESEARCH ARTICLE
10.1029/2023GB007844

Key Points:

- Porewater transition metal concentrations vary by up to an order of magnitude in aerobic pelagic clay sediments
- Most variability in porewater concentrations is observed in the top 5 cm
- Calculated benthic fluxes of most transition metals agree with estimated fluxes based on water column concentrations

Correspondence to:
Z. Steiner,
zsteiner@geomar.de

Citation:
Steiner, Z., Antler, G., Berelson, W. M., Crockford, P. W., Dunlea, A. G., Hou, Y., et al. (2023). Trace element geochemistry in North Pacific red clay sediment porewaters and implications for water-column studies. *Global Biogeochemical Cycles*, *37*, e2023GB007844. https://doi.org/10.1029/2023GB007844

Received 17 MAY 2023
Accepted 31 OCT 2023

Author Contributions:
Conceptualization: Zvi Steiner
Funding acquisition: William M. Berelson, Jess F. Adkins
Investigation: Zvi Steiner, Gilad Antler, Peter W. Crockford, Ann G. Dunlea, Yi Hou
Methodology: Zvi Steiner
Resources: Alexandra V. Turchyn, Eric P. Achterberg
Writing – original draft: Zvi Steiner
Writing – review & editing: Gilad Antler, William M. Berelson, Peter W. Crockford, Ann G. Dunlea, Yi Hou, Jess F. Adkins, Alexandra V. Turchyn, Eric P. Achterberg

Trace Element Geochemistry in North Pacific Red Clay Sediment Porewaters and Implications for Water-Column Studies

Zvi Steiner[1], Gilad Antler[2,3], William M. Berelson[4], Peter W. Crockford[5,6], Ann G. Dunlea[5], Yi Hou[7], Jess F. Adkins[8], Alexandra V. Turchyn[9], and Eric P. Achterberg[1]

[1]GEOMAR Helmholtz Centre for Ocean Research Kiel, Kiel, Germany, [2]Department of Earth and Environmental Sciences, Ben-Gurion University, Beer Sheva, Israel, [3]The Interuniversity Institute for Marine Sciences, Eilat, Israel, [4]University of Southern California, Los Angeles, CA, USA, [5]Department of Marine Chemistry and Geochemistry, Woods Hole Oceanographic Institution, Woods Hole, MA, USA, [6]Department of Earth Sciences, Carleton University, Ottawa, ON, Canada, [7]Department of Earth, Environmental, and Planetary Sciences, Rice University, Houston, TX, USA, [8]Department of Geology and Planetary Sciences, California Institute of Technology, Pasadena, CA, USA, [9]Department of Earth Sciences, University of Cambridge, Cambridge, UK

Abstract Geochemical analyses of trace elements in the ocean water column have suggested that pelagic clay-rich sediments are a major source of various elements to bottom-waters. However, corresponding high-quality measurements of trace element concentrations in porewaters of pelagic clay-rich sediments are scarce, making it difficult to evaluate the contributions from benthic processes to global oceanic cycles of trace elements. To bridge this gap, we analyzed porewater and bulk sediment concentrations of vanadium, chromium, cobalt, nickel, copper, arsenic, molybdenum, barium and uranium, as well as concentrations of the major oxidants nitrate, manganese, iron, and sulfate in the top 30 cm of cores collected along a transect from Hawaii to Alaska. The data show large increases in porewater concentrations of vanadium, manganese, cobalt, nickel, copper, and arsenic within the top cm of the sediment, consistent with the release of these elements from remineralized organic matter. The sediments are a sink for sulfate, uranium, and molybdenum, even though conditions within the sampled top 30 cm remain aerobic. Porewater chromium concentrations generally increase with depth due to release from sediment particles. Extrapolated to the global aerial extent of pelagic clay sediment, the benthic fluxes in mol yr^{-1} are Ba $3.9 \pm 3.6 \times 10^9$, Mn $3.4 \pm 3.5 \times 10^8$, Co $2.6 \pm 1.3 \times 10^7$, Ni $9.6 \pm 8.6 \times 10^8$, Cu $4.6 \pm 2.4 \times 10^9$, Cr $1.7 \pm 1.1 \times 10^8$, As $6.1 \pm 7.0 \times 10^8$, V $6.0 \pm 2.5 \times 10^9$. With the exception of vanadium, calculated fluxes across the sediment–water interface are consistent with the variability in bottom-water concentrations and ocean residence time of the studied elements.

1. Introduction

Studies of the distribution of trace elements and their isotopic composition in the oceanic water column repeatedly identify the sediment-water interface as a major vector in the cycle of a range of elements (Anderson, 2020; Homoky et al., 2016; Horner et al., 2021 and references therein). The upper sediment accumulates the remains of marine organisms and aeolian dust, exposing the particles to deep ocean pressure, temperature, and water chemistry. Slow accumulation rates of pelagic sediments allow thousands of years for meta-stable phases to dissolve, and for phases that are stable under the physico-chemical conditions prevailing in the abyssal ocean to precipitate (Andrews et al., 2020; Fantle & DePaolo, 2007). Common reactions that prevail in the upper 10–30 cm of abyssal North Pacific sediments include near-complete dissolution of calcium carbonate minerals, dissolution of some alumino-silicate minerals, and precipitation of authigenic clay minerals (e.g., Berger et al., 1976; Chen et al., 1988; Dunlea et al., 2017; Hein et al., 1979; Steiner et al., 2022b).

The top centimeters of marine sediments typically contain much more organic matter compared to the overlying water column, making surficial sediments a hotspot for heterotrophic bacterial activity (Parkes et al., 1994). Low water-to-solid ratios of the sediment column restrict water advection (Berner, 1980; Burdige, 2006). In coastal and continental shelf environments, the above conditions combine to allow oxygen to be readily depleted in porewaters. In contrast, pelagic sediments typically receive lower fluxes of organic matter and maintain aerobic conditions, at least in the top 50 cm (D'Hondt et al., 2015; Murray & Grundmanis, 1980), hence water-solid reactions occur under redox conditions that often resemble the deep ocean. Together, these factors typically result

in geochemical gradients across the sediment-water interface being smaller in pelagic sediments than in coastal sediments. However, an additional consequence is that benthic fluxes in the pelagic environment should be representative of the actual transport between sediment and bottom waters because there is a minimal redox gradient in the upper sediment column; hence, little oxidation is expected once metals diffuse between the oxidized sediment and bottom waters. Furthermore, deep sea sediments can generally be treated as diffusive transport dominated (Boudreau et al., 2020).

Microbial communities adapt to heterogeneous redox conditions by utilizing the most energy-efficient electron transport option available, generally in the order of $O_2 > NO_3^- > MnO_2 > Fe(OH)_3 > SO_4^{2-} > CH_2O$ (Arndt et al., 2013; Froelich et al., 1979). Most transition metals and many other elements are directly or indirectly affected by changing redox conditions induced by microbial respiration (e.g., Bennett & Canfield, 2020; Crusius et al., 1996; Little et al., 2015; Morford & Emerson, 1999; Smrzka et al., 2019; Tribovillard et al., 2006). For example, cobalt (Co) has similar attributes to manganese (Mn) and can be reduced to Co^{2+} and oxidized to Co^{3+} by similar enzymes as those transforming Mn between the Mn^{2+}, Mn^{3+} and Mn^{4+} oxidation states (Moffett & Ho, 1996). Barium (Ba), vanadium (V), molybdenum (Mo), nickel (Ni) and copper (Cu) tend to adsorb to Mn oxides and are released back to the water when Mn oxides are reduced (Hein et al., 2020; Tribovillard et al., 2006), and iron (Fe), Mo, V, Ni, U, and Co co-precipitate with sulfide minerals under anoxic conditions (Algeo & Liu, 2020; Morford & Emerson, 1999). Barium is also influenced by the formation and dissolution of barite ($BaSO_4$), and is thus affected by microbially mediated reduction and oxidation of sulfate (McManus et al., 1998) and ion exchange (Middleton et al., 2023).

The majority of the chemical and biological reactions that determine the fluxes between sediments and bottom waters take place within the top meter of the sediment column (e.g., Klinkhammer, 1980; Sayles, 1979; Scholz et al., 2011), and the geochemistry of many trace elements is extremely active in the top few centimeters of marine sediments (e.g., Andreae, 1979; Heggie & Lewis, 1984; Heggie et al., 1986; Klinkhammer, 1980; Shaw et al., 1990). Yet, high-resolution trace metal data from the upper meter of red clay sediments are scarce (Klinkhammer, 1980; Klinkhammer et al., 1982; Sawlan & Murray, 1983). Moreover, the sequence of redox, mineral dissolution, and precipitation reactions in red clay sediments is poorly constrained. Since pelagic clay sediments cover a third of the global ocean seafloor (Diesing, 2020; Dutkiewicz et al., 2015), this represents a gap in our understanding of the marine cycling of a broad spectrum of elements. This study aims to address this gap by providing high-resolution dissolved trace element data from short sediment cores along a transect from Hawaii to Alaska. The sediments underlie regions of variable surface ocean biogeochemical conditions, from the oligotrophic subtropical gyre to the productive subpolar gyre of the North Pacific. This wide spatial coverage hence provides constraints on the effect of varying pelagic sedimentation regimes on trace metal cycling and fluxes between pelagic red clay sediments and deep waters of the abyssal North Pacific.

2. Materials and Methods

2.1. Sampling

Short sediment cores with overlying water were collected in August 2017 at five North Pacific stations, from Hawaii Ocean Time-series Station ALOHA (Station 1) to 49°50.4′N 149°37.7′W (Station 5; 4.6 deg west of Ocean Station Papa) during cruise CDisK-IV on board the R/V Kilo Moana (Figure 1 and Table 1). An eight-barrel multi-corer (Ocean Instruments 800 multi-corer with 9.6 cm inner diameter polycarbonate liners) was used for the core collection. The core liners were pre-drilled down the length of the core tube (75 cm) and covered with electrical tape. The cores were taken to a cold-room laboratory immediately after retrieval. Porewaters were extracted from two cores from each multi-corer cast with undisturbed sediment-water interfaces using Rhizon samplers. The Rhizon samplers were inserted every two cm top to the bottom after draining the overlying water. Samples from core number 1 were primarily used for nutrient analyses. Approximately 20 mL of porewater was extracted using each Rhizon sampler, the samples were then re-filtered using 0.45 µm syringe filters, and the nutrient samples were frozen at −18°C until analyses of totally oxidized nitrogen (nitrate + nitrite) at the University of Maryland Nutrient Analytical Services Lab (Salomons, MD, USA). Rhizons inserted into core number 2 were acid-cleaned with 0.001 N HNO_3 for at least 24 hr, washed with de-ionized water (Milli-Q, Millipore) and kept in de-ionized water until use. The first 1 mL extracted was discarded, and the next 2 mL were stored in acid cleaned polypropylene (PP) vials. Aliquots designated for trace and major element analyses were acidified with double distilled HNO_3 to final acid concentration of 0.035 M shortly after the porewater separation. Sulfur (as

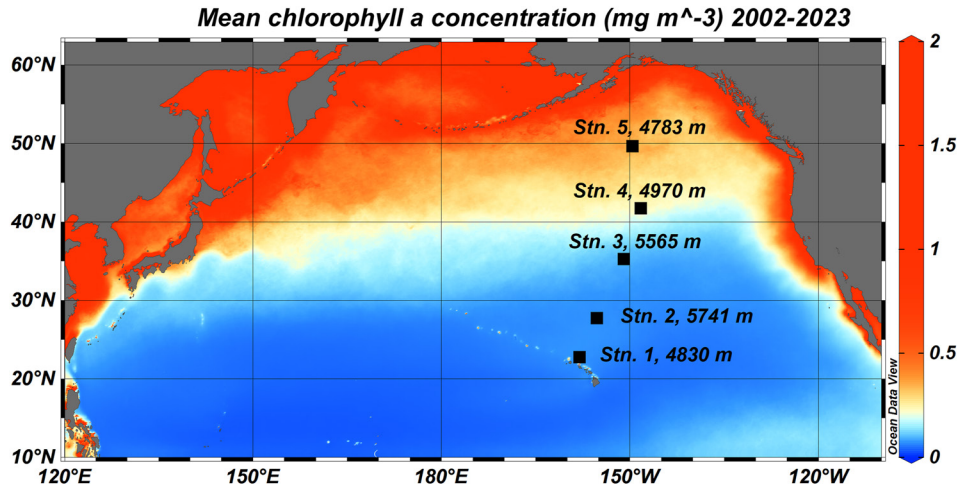

Figure 1. Station location and bottom water depths. Map plotted using Ocean Data View 5.6.3 (Schlitzer, 2020), mean surface chlorophyll-*a* concentration for the period July 2002 to May 2023 are from Nasa Aqua-MODIS satellite data (https://oceancolor.gsfc.nasa.gov).

sulfate, SO_4^{2-}) concentrations were analyzed in acidified samples from both cores and averaged for each depth horizon. Silicic acid concentrations in these sediment cores were previously published by Hou et al. (2019) and porewater concentrations of NO_3^-, Ca^{2+}, K^+, Sr^{2+}, Mg^{2+}, and Li^+ are provided in Steiner et al. (2022b).

2.2. HR-ICP-MS

Samples were diluted 1:20 in 1 M HNO_3 and analyzed at GEOMAR Helmholtz Center for Ocean Research Kiel using an Element-XR high resolution sector field inductively coupled plasma mass spectrometer (HR-ICP-MS; Thermo Fisher Scientific) in medium resolution (R = 4,000) for ^{51}V, ^{52}Cr, ^{55}Mn, ^{56}Fe, ^{59}Co, ^{60}Ni, ^{63}Cu, ^{95}Mo, ^{98}Mo, ^{137}Ba, ^{138}Ba, ^{238}U, and in high resolution (R = 10,000) for ^{75}As, allowing isobaric interferences to be resolved. Calibration standards were prepared by spiking a North Pacific deep-water sample with single element standard solutions supplied by Inorganic Ventures. The samples were analyzed in duplicate, and a consistency standard was analyzed every nine samples for drift correction. To verify that none of the profiles were the result of uncorrected drift, the sample order was randomized, and the instrument recalibrated before analyses of the duplicate samples. The average difference between duplicate analyses (n = 60) was V 2%, Cr 4.6%, Mn 3.7%, Fe 2.4%, Co 5.6%, Ni 10.3%, Cu 2.8%, Mo 1.1%, Ba 0.8%, As 6.8%, and U 1.0%.

2.3. Sulfate

Sulfate (SO_4^{2-}) to sodium (Na^+) ratios were analyzed at the University of Cambridge using an Agilent Technologies 5100 inductively coupled plasma optical emission spectroscopy following the method of Steiner

Table 1
Station Information, Porosity, and Mean Grain Size of the Top Sediment Layer

	Lat (°N)	Long (°W)	Bottom depth (m)	φ[a] (0–1 cm)	$D_{0.5}$[b] (μm)	Sed. rate[c] (cm ka^{-1})	Bioturbation rate[c] (cm^2 yr^{-1})
Station 1 (ALOHA)	22°45.9′	157°58.5′	4,830	0.865	6.7	0.44	0.007
Station 2	27°45.8′	155°15.3′	5,741	0.823	3.3	0.11	0.008
Station 3	35°16.8′	150°59.8′	5,565	0.855	3.7	0.23	0.004
Station 4	41°43.5′	148°17.5′	4,970	0.887	4.6	0.15	0.45
Station 5	49°50.4′	149°37.7′	4,783	0.784	28	0.57	0.020

[a]Porosity data (φ) are from Hou et al. (2019). [b]$D_{0.5}$ are the median grain size of the top sediment layer (0–1 cm), analyzed by laser using a Malvern Instruments Mastersizer 2000 following treatment with 30% H_2O_2 to remove organic matter and dispersion with 4.4% sodium hexametaphosphate. [c]Sediment accumulation and bioturbation rates from Kemnitz et al. (2022).

et al. (2020). The samples were diluted with 0.16 M HNO_3 to a salinity of 0.43, and analyzed in duplicate employing sample-standard bracketing. The calibration was undertaken using different dilutions of IAPSO North Atlantic seawater standard from batch P157 (https://osil.com/product/p-series). Concentrations of SO_4^{2-} and Na^+ in the IAPSO standard were assumed to be similar to average seawater concentrations (Burton, 1996). Sulfate was measured as total sulfur on the ICP-OES; we assume it is mostly sulfate as we immediately acidified the samples. Sulfate concentrations are reported as SO_4^{2-}/Na^+ ratios to eliminate variability related to instability in the plasma flow, sample introduction system or dilutions. The average difference between SO_4^{2-}/Na^+ of duplicate analyses ($n = 59$) was 0.36%.

Porewater sulfate was precipitated as barite ($BaSO_4$) using a barium chloride solution for the determination of its sulfur isotope ratio ($\delta^{34}S$) through combustion in a Flash Element Analyzer (Flash EA) coupled by continuous flow to a Delta Advantage mass spectrometer at the University of Cambridge in the Godwin Laboratory for Paleoclimate research. Samples were bracketed by seawater standard NBS127 with a $\delta^{34}S$ value of 20.3‰ and are reported relative to the international standard V-CDT. The standard deviation of the NBS127 runs was 0.05‰; the long-term standard deviation of this method is 0.3‰.

2.4. Total Digestions

Major and trace element concentrations of marine sediment collected during the CDisK-IV cruise were analyzed at Woods Hole Oceanographic Institution (WHOI). Samples were first lyophilized for over 24 hr, and then cooked in a heated acid cocktail (HNO_3, HCl, and HF) with later additions of H_2O_2 before being dried down, redissolved with HNO_3 and H_2O_2 and diluted. Sample solutions were analyzed on the Thermo iCAP ICP-MS in the WHOI Plasma Facility. The precision of the analyses was 3% for the reported elements determined by digesting two samples in triplicates and calculating the standard deviation divided by the average (relative standard deviation, RSD) of the triplicates.

2.5. Bulk Sediment Carbon

Sediment total carbon content was determined from dried and ground sediment powder through combustion in an element analyzer (Costech) coupled to a 2131i Picarro Cavity Ring Down Spectrometer. Then, total inorganic carbon was analyzed by weighing and acidifying ground sediment powder with 10% phosphoric acid in exetainer test tubes. The evolved CO_2 was measured using the Picarro 2131i Spectrometer. Total CO_2 was standardized by running known masses of optical-grade calcite standard material. Total organic carbon (OC) was determined as the difference between the total carbon and total inorganic carbon.

3. Results

3.1. Description of the Cores

The southern stations (Stations 1–3) underlie the highly oligotrophic subtropical gyre of the North Pacific, and the northern stations (Stations 4–5) underlie the far more productive subpolar gyre. The transition zone between the subtropical and subpolar gyres typically shifts between 32°N in winter and 42°N in summer (Ayers & Lozier, 2010). All sediment samples collected for this study are low in organic matter (Figure 2a), classified as red clays and contain <1% $CaCO_3$ (Figure 2b; Steiner et al., 2022b). The cores from Stations 4 and 5 underlying the subpolar gyre contain 2.5%–8% biogenic silica, while the biogenic silica content of cores from Stations 1–3 is <1.2% (Figure 2c; Hou et al., 2019). There was a "fluff" layer on top of some of the cores from Station 4, which was composed of fresh organic matter and biogenic silica, likely derived from recent sinking of a diatom bloom. There were also visible signs of bioturbation at Stations 4 and 5, but not at Stations 1–3. The tops of cores from Stations 2, 3 and 4 contained sporadic Mn nodules, 1–4 cm in diameter. The core tops from Station 5 contained several rocks, 1–2 cm in diameter, with mineral composition consistent with an igneous source (quartz, feldspar, plagioclase, Ca poor pyroxene, phyllosilicate, and small amounts of apatite, pyrite, calcite and titanite). The mean grain size of the sediment samples from Stations 1–4 is 3.1–6.7 μm, but sediment samples from Station 5 are much coarser with an average grain size between 22 and 28 μm (Table 1). A different sedimentary regime at Station 5 is also reflected by a lower bulk sediment aluminum (Al) content compared to the other stations (Figure 2d). Sediment accumulation rates vary between 0.11 cm ka^{-1} at Station 2

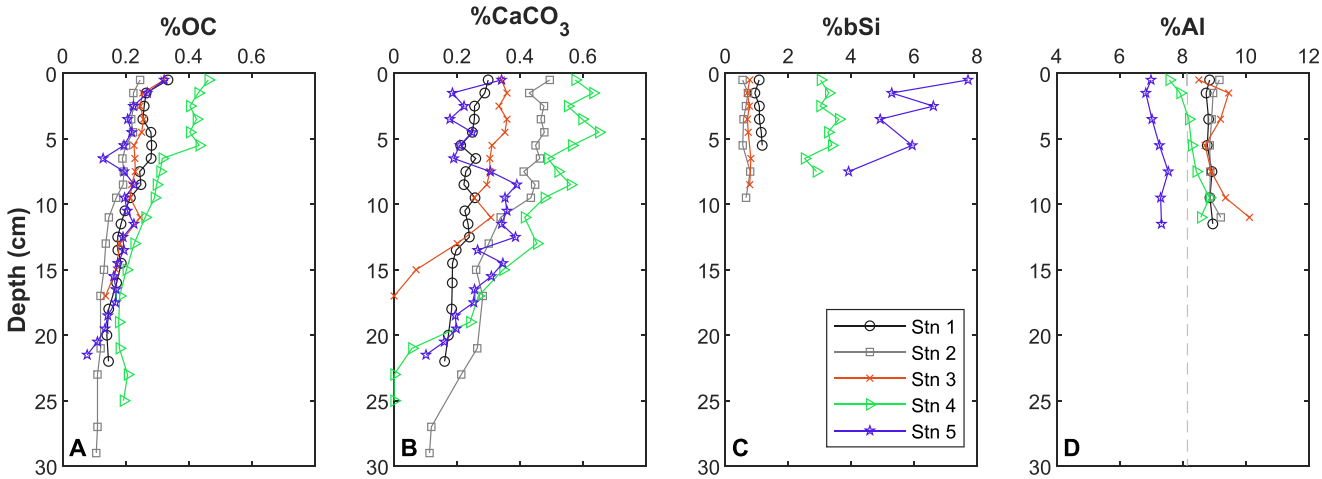

Figure 2. Bulk sediment content of (a) organic carbon, (b) calcium carbonate (Steiner et al., 2022b), (c) biogenic silica (Hou et al., 2019), and (d) aluminum. The vertical dashed line in D represents the average Al content of the upper continental crust (Rudnick & Gao, 2003).

to ~0.6 cm ka^{-1} at Station 5 (Kemnitz et al., 2022); these sedimentation rates are within the range characteristic of North Pacific red clays (0.05–0.6 cm ka^{-1}), and higher than the average sedimentation rates of South Pacific red clays (~0.04 cm ka^{-1}) (Glasby, 1991).

3.2. Trace Metals Content of the Porewater and Sediment

Figure 3 presents the main organic matter oxidants: total oxidized nitrogen (nitrate + nitrite), Mn, Fe, and SO_4^{2-}. Porewater total oxidized nitrogen concentrations increase in the top several cm of all cores and do not decrease in the depth range studied. Porewater Mn and Fe concentrations are in the nanomolar range, and bulk sediment Mn and Fe content are higher than the average upper continental crust (UCC) composition, consistent with the prevalence of aerobic conditions in the studied cores. Despite evidence that oxygen was not fully depleted, the porewater SO_4^{2-}/Na^+ decreases by up to 3% relative to the overlying water concentration. Although with this decrease we cannot resolve the microbial sulfate reduction from the release of Na from ion exchange reactions on clay minerals, microbial sulfate reduction seems a more parsimonious explanation because the clay minerals have been in contact with seawater for millennia. Notwithstanding the measured depletions in SO_4^{2-}/Na, there is no evidence for presence of free H_2S in the top 30 cm of the sediments observed here, and Andreae (1979) could not detect H_2S in the top 70 cm of a core collected at a location close to our Station 3. The measured variability of porewater sulfur isotope ratios was within the precision of the analytical method (Figure 3g).

We divide analyzed trace elements into three groups based on their function in marine porewaters and the shape of their profiles. Group I (Figure 4) includes elements that exhibit a sharp concentration peak at the top cm of the sediment, V, Ni, Cu, and arsenic (As). These elements are redox sensitive, and they are all active participants in biological cycling (Andreae, 1979; Ho et al., 2003; Horner et al., 2021; Martinez-Ruiz et al., 2019). A subsurface concentration peak was also observed in the Mn data (Figure 3b). Below the subsurface peak, porewater concentrations of the group I elements tend to stabilize at lower-than-bottom-water concentrations in cores underlying the subtropical gyre, whereas higher than bottom-water concentrations are maintained in cores underlying the subpolar gyre.

Bulk sediment concentrations of V, Ni, and Cu are higher than the average UCC concentration (Figures 4e–4g). This feature is particularly pronounced for Cu, where the average sediment content is elevated by a factor of seven compared to UCC. Subpolar gyre Station 5 contrasts with the other stations as it has lower Ni and Cu concentrations. The sediment V content of Station 1, and to a lesser degree Station 5, are elevated compared to the other stations, possibly due to proximity to volcanic sources.

Group II (Figure 5) includes elements whose concentrations gradually decrease as a function of depth in the sediment, Mo and uranium (U). By the shape of the profile, SO_4^{2-} (Figure 3d) also belongs to group II, as is As in the deeper part of the cores (Figure 4d). The largest decreases in the concentrations of SO_4^{2-}, U, Mo, and

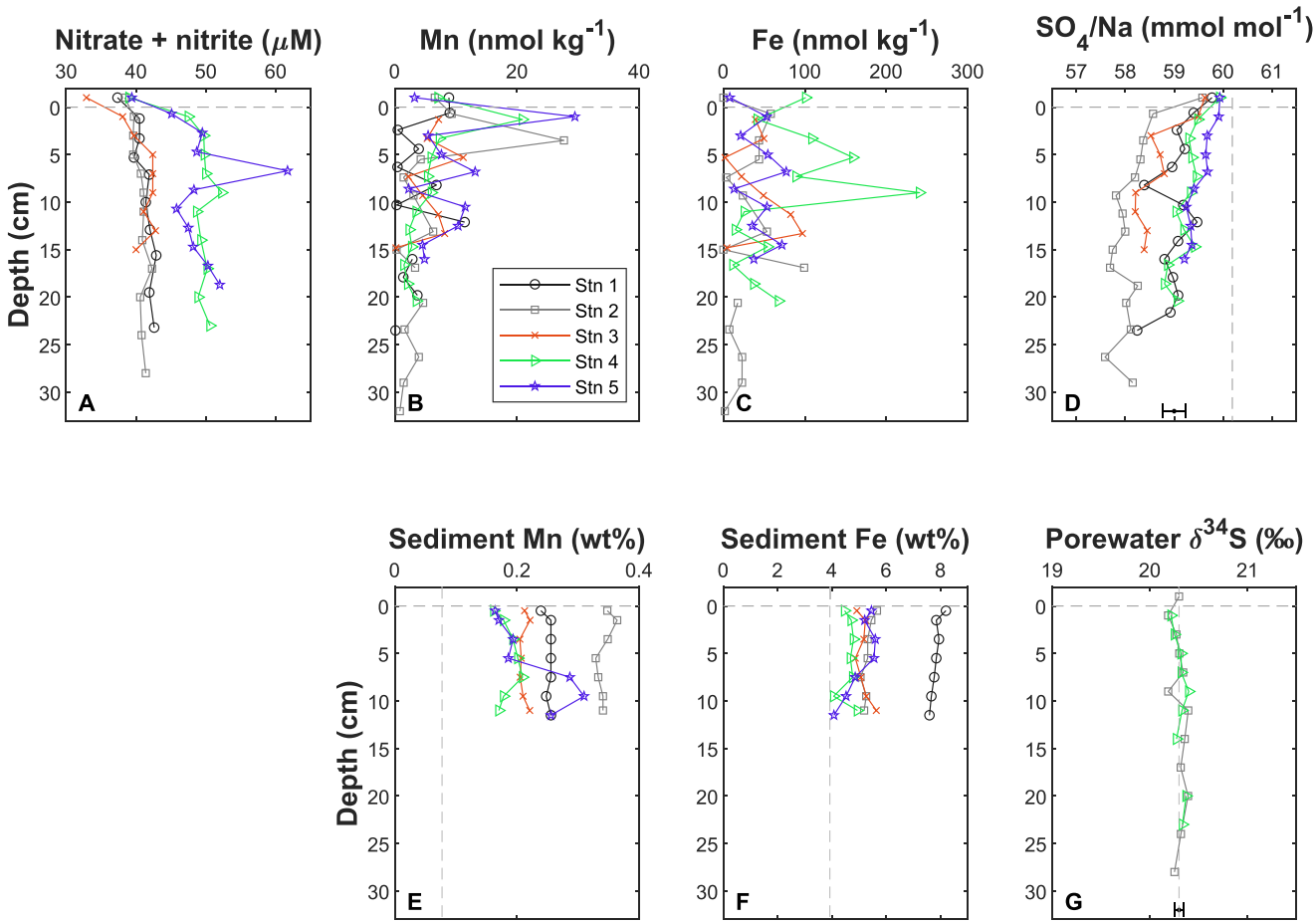

Figure 3. Main organic matter oxidants. (a–d) Porewater concentrations of total oxidized nitrogen, manganese, iron, and sulfate-to-sodium ratio. Overlying water concentrations are marked one cm above the sediment-water interface. The vertical dashed line in (d) represents the mean ocean SO_4/Na ratio assumed for the IAPSO standard used for calibration and drift correction (Burton, 1996). Error bar in D illustrates $\pm 1\sigma$ SD around the mean concentration of all samples as determined from duplicate analyses of the samples ($n = 60$). Error bars are less than the symbol size for (a–c). Note that the error bars refer only to the analytic precision and do not account for the modification of sample chemistry during core retrieval, porewater extraction and preservation of the samples. (e, f) Bulk sediment Mn and Fe; the vertical dashed lines in (e) and (f) represent the average composition of the upper continental crust (Rudnick & Gao, 2003). (g) $\delta^{34}S$ of porewater from Stations 2 and 4, the vertical dashed line in G represents the $\delta^{34}S$ of the seawater standard.

As are observed in Station 2, followed by Stations 1 and 3. Stations 1–3 underlie the oligotrophic subtropical gyre, and Station 2 is the deepest station in this study and underlies low productivity surface waters (Dong et al., 2019, 2022). The bulk sediment content of Mo and U differ compared to the average UCC as Mo is slightly enriched in these cores, and its concentrations increase between 5 and 12 cm (Figure 5c), while U concentrations are ≤UCC (Figure 5d).

Group III includes elements with unique depth profiles that do not easily fit into any of the other groups, Co, chromium (Cr), and Ba (Figure 6). At Station 4, the concentrations of Cr and Ba peak in the upper porewater sample, 1.3 cm below the sediment-water interface, analogous to the group I elements, and Co concentrations are high compared to the other stations and reach a peak concentration 6 cm deeper (Figure 6). Despite the unusual profile of Station 4, we hereafter discuss Co in the context of the Group I elements due to our a priori expectation that Co geochemistry is typically related to Mn (Moffett & Ho, 1996), and due to the rough agreement between the shape of the Co concentration profiles in the other stations (Figure 6d) and the Group I elements (Figure 4). The porewater geochemistry of Cr is unusual among the elements studied here, it is the only element that is clearly diffusing up from the studied sediment depth (Figures 6b and 6e); a deep Cr source is particularly evident at Station 1 (ALOHA). The porewater concentrations of Ba increase in the top few cm of the sediment compared with bottom water concentrations (Figure 6c). Porewater Ba concentrations reach higher values in the cores underlying the subpolar gyre and decrease deeper in the core. Bulk sediment Ba concentrations are higher than

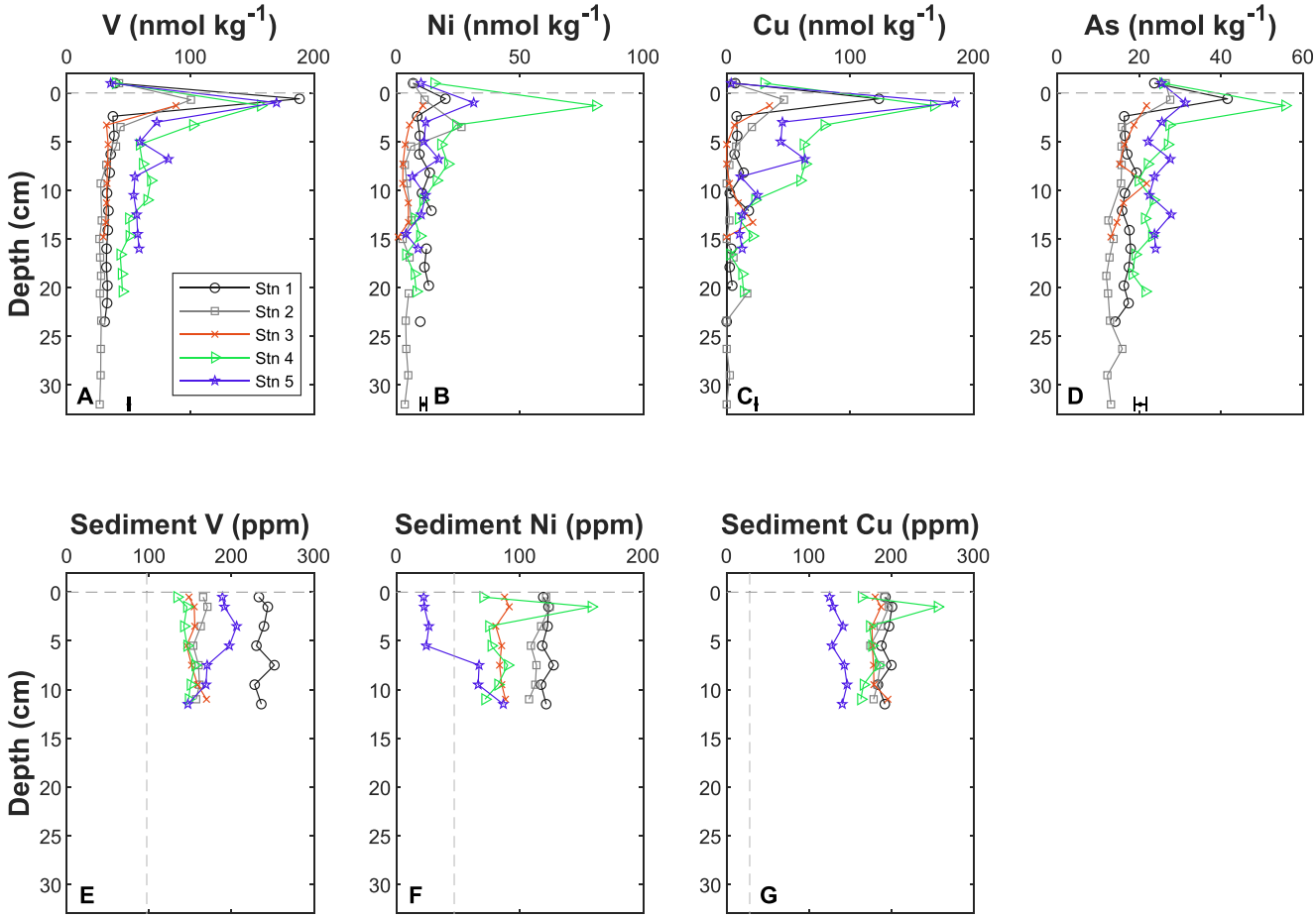

Figure 4. Vanadium, nickel, copper and arsenic. (a–d) Porewater concentrations. Error bars illustrate the analytic $\pm 1\sigma$ SD. (e–g) Bulk sediment concentrations. The vertical dashed lines in (e–g) represent the average composition of the upper continental crust.

average UCC (Figure 6i), the largest enrichment was measured in Station 4 followed by Station 5, and smaller enrichments were measured in cores underlying the subtropical gyre.

4. Discussion

Porewaters were collected in this study from oxygenated sediments. Nevertheless, trace metal distributions vary greatly with depth and are not merely a function of their redox potential. In the following subsections, we discuss the dominant processes controlling metal release and uptake from the surface to the deeper sediment. This discussion is followed by the calculation of element fluxes between the sediment and bottom water, and we conclude by outlining the implications of our findings for element cycles in the modern ocean.

4.1. Top Core Release of Redox Sensitive Elements

The concentrations of group I elements Mn, Co, V, Ni, Cu, and As peak in the upper porewater samples (Rhizon sampler typically inserted one cm below the sediment-water interface) (Figure 4). The nitrate data suggest that the redox characteristics of some of these group I elements does not explain the near surface peak in their porewater concentrations. Nitrate + nitrite concentrations increased in the top 5 cm of these cores and remained constant to the bottom of our sampling interval, which indicates that oxygen is still available for microbial respiration and that redox conditions are similar to those of the oceanic water column (Figure 3a). Porewater enrichments in V, Ni, Cu, As, and Ba relative to the overlying water that are larger than the variability in Mn concentrations (Figures 3b, 4, 6c) suggest that partial dissolution of Mn nodules is also less likely to explain the porewater enrichment of these elements. The minor enrichment in porewater Mn concentrations near the surface further suggests that upward diffusing Mn is insufficient to induce the formation of the Mn nodules found on top of some of these cores.

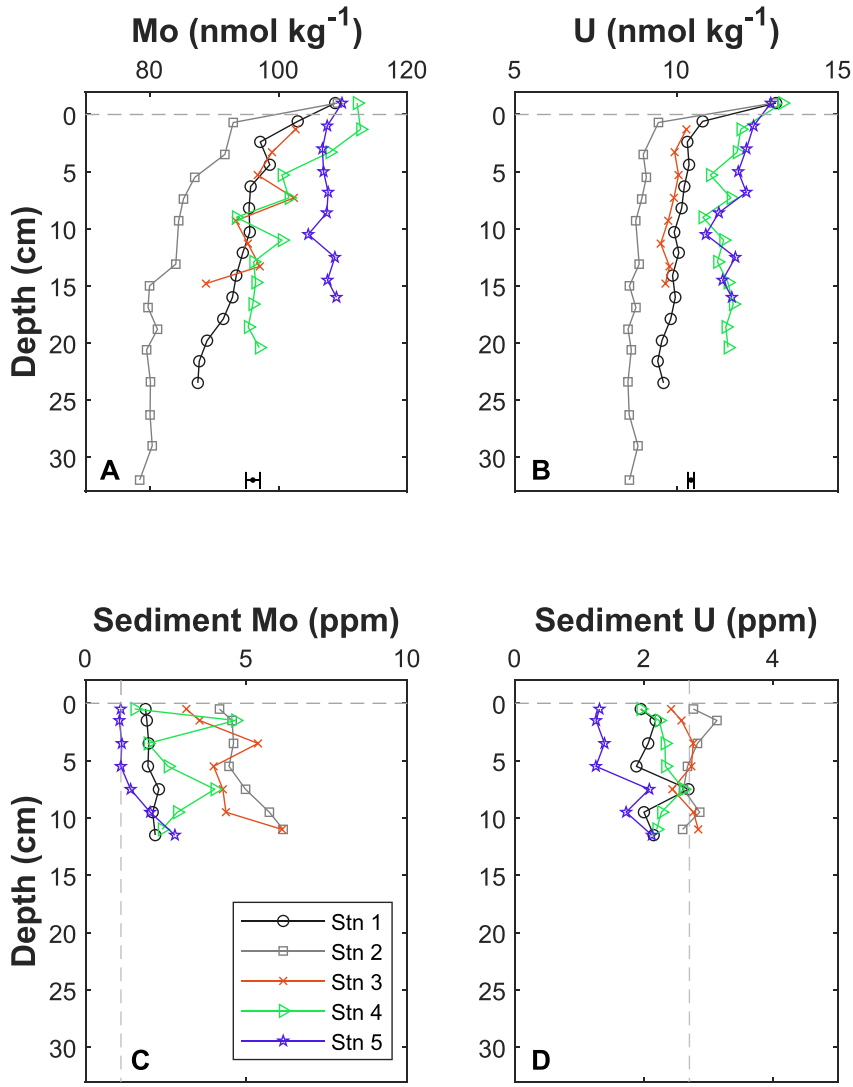

Figure 5. Molybdenum and uranium concentrations. (a, b) Porewater profiles. Error bars illustrate the analytical error $\pm 1\sigma$ SD. (c, d) Bulk sediment profiles; the vertical dashed lines represent the average composition of the upper continental crust.

Instead, the nodules in this region are formed by metals from the overlying water column (i.e., hydrogenous, not diagenetic). This result supports findings of a similar survey in the Mn nodule-rich central equatorial Pacific (Klinkhammer et al., 1982). It is worth mentioning that relative to UCC the sediment is enriched in all group I elements as well as Co and Ba. With regard to Mn, this enrichment is consistent with the expected stability of Mn oxides under aerobic conditions. Positive linear correlations between the sediment content of Mn with Co ($R^2 = 0.31$) and Ni ($R^2 = 0.28$) suggest that part of the excess sedimentary Co and Ni is adsorbed to Mn oxides. The correlation of other elements with the Mn content of the sediment is very weak, and in the case of Ba, it is negative.

In the water column, V, Co, Ni, Cu, Ba, Cr, and As exhibit nutrient-like or bio-intermediate profiles, supporting inferences of their uptake in association with organic matter production in the surface ocean and net release in waters below the photic zone upon organic matter remineralization (Ho et al., 2018; Horner et al., 2015; Moos & Boyle, 2019; Saito et al., 2010; Wurl et al., 2015; Zheng et al., 2019, 2021). To further investigate the biogeochemical processes of nutrient-like elements once deposited in marine sediments, we used a simple calculation that accounts only for nutrient release and diffusion to test whether organic matter remineralization explains the observed increases in porewater Ni, Cu and Co concentrations (Klinkhammer et al., 1982):

$$\frac{M}{N} = \frac{(M_1 - M_0) \cdot D_M}{(N_1 - N_0) \cdot D_N} \quad (1)$$

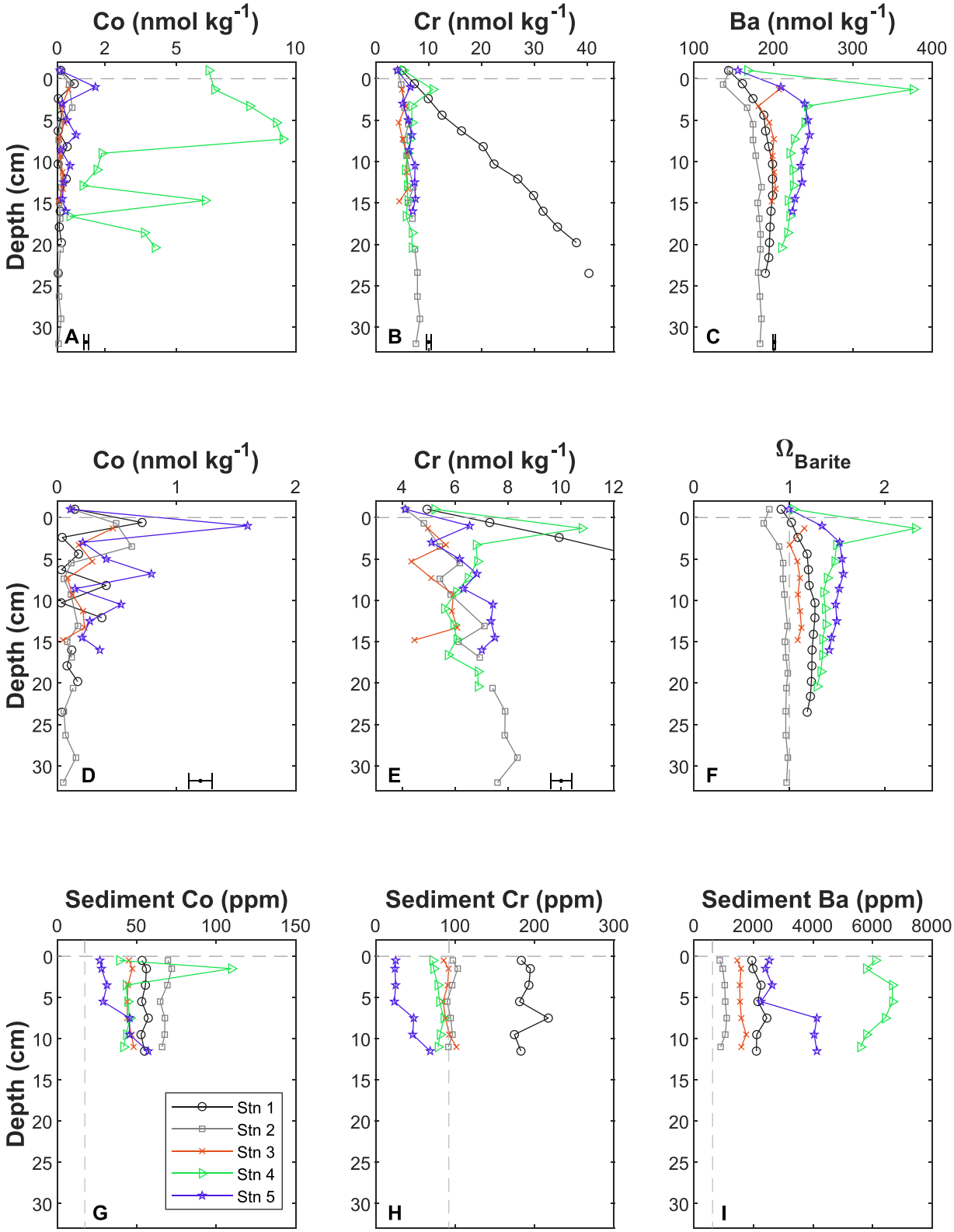

Figure 6. Cobalt, chromium and barium. (a–c) Porewater concentrations. Subplots (d) and (e) focus on the relevant concentration range of cobalt and chromium at four of the five stations. (f) Porewater saturation state with respect to barite ($BaSO_4$), equilibrium saturation ($\Omega_{Barite} = 1$) is marked with a vertical dashed line. Error bars illustrate the analytic $\pm 1\sigma$ SD. (g–h) Bulk sediment concentrations; the vertical dashed lines represent the average composition of the upper continental crust.

Table 2
Calculated Metal-To-Nitrate Enrichment of the Upper Porewater Samples Relative to the Overlying Water Concentrations, Calculated Using Equation 1

	Mn/NO_3 (mmol mol^{-1})	Co/NO_3 (mmol mol^{-1})	Ni/NO_3 (mmol mol^{-1})	Cu/NO_3 (mmol mol^{-1})	Cr/NO_3 (mmol mol^{-1})	As/NO_3 (mmol mol^{-1})	V/NO_3 (mmol mol^{-1})	Ni/Si (mmol mol^{-1})
Station 1	0.01	0.06	1.3	13	0.4	2.4	22	0.49
Station 2	0.7	0.10	1.2	11	0.3	0.4	21	0.28
Station 4	0.5	0.27	2.7	7	0.3	1.5	7	0.44
Station 5	1.5	0.09	1.2	11	0.2	0.4	11	0.19
Average	0.7 ± 0.4	0.13 ± 0.07	1.6 ± 0.5	11 ± 2	0.3 ± 0.1	1.2 ± 0.8	15 ± 6	0.35 ± 0.12
Twining and Baines (2013)*		0.002	0.06	0.03				
Twining et al. (2012)								0.03

Note. *Twining and Baines (2013) summarized metal to P ratios of North Pacific single cells in their Table 3, these ratios were converted to nitrate assuming $N/P = 16$.

Here M is metal, N is NO_3^-, the subscripts 1 and 0 refer to the upper porewater sample and bottom water, D_M and D_N are the diffusion coefficients of the metal and nitrate, respectively (Table 3; Li & Gregory, 1974). Our calculated M/N ratios using Equation 1 are much higher than single-cell stoichiometries from the North Pacific (Table 2). Cellular quotas of trace metals vary by more than an order of magnitude between species and study sites (Ho et al., 2003; Twining & Baines, 2013); however, our results are consistent for all studied elements, indicating that the intracellular metal content of material raining from the surface ocean is too low to explain the porewater concentrations of these elements. Preferential remineralization of N over metals in sinking particles may contribute to the high observed M/N ratios in our pore fluids (Boyd et al., 2017; Smith et al., 1992).

Twining et al. (2012) demonstrated that Ni adsorption by diatom frustules is as important as Ni uptake by living plankton cells. Comparison of Ni/Si ratios of the porewater samples with Ni/Si of fresh biogenic silica suggests that this could account for another 10% of the excess Ni in the upper porewater samples (Table 2).

Apart from association with living organisms, Fe-Mn oxy-hydroxides and biogenic silica, trace metals can also be transported to the sediment via terrigenous lithogenic material, $CaCO_3$ shells and by adsorption to settling organic matter. Most $CaCO_3$ produced along the cruise transect dissolves before burial in the sediment, hence $CaCO_3$ dissolution does not contribute significantly to the porewater chemistry of these cores (Steiner et al., 2022b). Adsorptive scavenging to particulate matter is an important component of the marine cycle of Cu and Co (Bruland, 1980; Hawco et al., 2018; Hayes et al., 2018; Roshan et al., 2020; Takano et al., 2014), and the porewater enrichment of these elements suggest that the release of scavenged Cu and Co shortly after burial is a source of dissolved Cu and Co to the bottom waters. Adsorptive scavenging to organic matter is probably less important for Ni and V (Cameron & Vance, 2014; Collier, 1984; Sclater et al., 1976) but Ni and V can adsorb and precipitate with Mn and Fe oxides (Hein et al., 2020; Wehrli & Stumm, 1989).

Table 3
Diffusive Fluxes Across the Sediment-Water Interface

	Ba^{2+} (nmol m^{-2} d^{-1})	Mn^{2+} (nmol m^{-2} d^{-1})	Co^{2+} (nmol m^{-2} d^{-1})	Ni^{2+} (nmol m^{-2} d^{-1})	Cu^{2+} (nmol m^{-2} d^{-1})	CrO_4^{2-} (nmol m^{-2} d^{-1})	UO_2^{2+} (nmol m^{-2} d^{-1})	$H_2AsO_4^-$ (nmol m^{-2} d^{-1})	MoO_4^{2-} (nmol m^{-2} d^{-1})	VO_4^{2-} (nmol m^{-2} d^{-1})	SO_4^{2-} (nmol m^{-2} d^{-1})
D_m (µcm^2 s^{-1})[a]	3.87	2.94	3.25	2.99	3.27	4.92	1.89	4.01	4.39	4.39	4.79
Station 1	20	0.1	0.55	12	110	3.5	−1.3	21	−7.6	200	−90
Station 2	−9	2.1	0.32	4	36	0.9	−1.8	1	−19	67	−590
Station 3	69	0.5	0.33	3	28	1.2	−1.5	−5	−8.3	59	−56
Station 4	260	13	0.25	62	140	8.7	−0.8	38	0.8	160	−540
Station 5	49	18	1.13	15	140	2.8	−0.2	5	−2.4	140	190
Average	77	6.7	0.51	19	92	3.4	−1.1	12	−7.2	120	−220
SE	72	7.0	0.26	17	48	2.1	0.5	14	5.2	49	280

Note. Positive fluxes are in the direction from the sediment to the bottom-water.
[a]Free solution molecular diffusion coefficient (D_m) at 1°C was calculated following Li and Gregory (1974).

Among the group I elements, the Station 4 porewater profile of Co is distinctive (Figure 6a). High porewater Co concentrations at Station 4 align well with observations that deep water Co concentrations near this site are high (Chmiel et al., 2022) and identify the sediment as an important source of Co to the bottom water. Except for one sample, the Co content of Station 4 sediment is not distinct (Figure 6g), suggesting that the porewater and water column anomalies are associated with phases that are not preserved in the sediment. The porewater Co profile shape and concentration range at Station 4 are similar to published porewater profiles from San Nicolas, Santa Cruz and San Clemente basins in the California Margin (Shaw et al., 1990). The difference is that in the California Margin, elevated Co concentrations are observed in the Mn reduction zone, and porewater Mn concentrations are >3 orders of magnitude higher than Co. The correlation between Co and Mn concentrations is expected because Co^{3+} tends to coprecipitate with MnO_2, and the same bacterial enzymes that oxidize Mn^{2+} to insoluble Mn^{4+} can readily oxidize soluble Co^{2+} to insoluble Co^{3+} (Moffett & Ho, 1996).

The elevated porewater Co concentrations at Station 4 may be related to the presence of an organic matter and biogenic silica rich layer on top of the sediment (Hou et al., 2019). Kellogg et al. (2020) have shown that common northeast Pacific diatoms can efficiently substitute zinc (Zn) with Co and grow in Zn deficient waters with little or no reduction in growth rate, an adaptation to the unusually high Co/Zn ratios in the northeast Pacific surface waters. Therefore, the Co content of northeast Pacific diatoms can be much higher than the Co content of Atlantic diatoms (Kellogg et al., 2020). The elevated Ni content of Station 4 porewaters (Figure 4b) further supports the notion that the elevated pore- and overlying water Co concentrations in Station 4 result from decomposing diatoms. The Ni content of diatoms is much higher than other common phytoplankton (Twining et al., 2012); hence, the dissolution of diatom material should release Ni in excess of inorganic nitrogen. Another specific source of elevated porewater Ni and Co can be traced to a sediment layer 1–2 cm below the sediment interface (Figures 4f and 4g); however, the Ni- and Co-rich horizon is not higher in biogenic silica than other sediment layers in the same core (Figure 2c). This suggests that either the excess biogenic silica was solubilized and the excess metals remained in the sediment or there is an anthropogenic source for the elevated metal concentrations. An anthropogenic source of excess lithium from north Chinese coal has been demonstrated for surface water samples from Station 4 (Steiner et al., 2022a), and it is possible that the same source can also supply Ni and Co in excess of natural levels, but it is not likely that anthropogenic contamination would be observable in such slowly accumulating deep-sea sediments. An anthropogenic source is also inconsistent with the observation that dissolved Co is high in the entire deep-water profile at this region (Chmiel et al., 2022), given the age of the Pacific deep-water.

4.2. Processes Deeper in the Cores

In oxygenated waters, both Mo and U are found in +6 oxidation states and form highly soluble oxyanions (Calvert & Pedersen, 1993; Morford et al., 2005; Smedley & Kinniburgh, 2017). In their reduced +4 oxidation state, U and Mo tend to precipitate out of solution. Reduction of UO_2^{2+} to the particle reactive U^{4+} oxidation state involves inorganic reduction by Fe sulfide minerals and bacterial activity (Bargar et al., 2013; Sharp et al., 2011), an observation that explains why the decrease in porewater U concentration is normally observed around the depth of maximum reduced Fe concentrations (Cochran et al., 1986). Molybdenum is typically reduced deeper in the sediment relative to Fe; reduction of Mo involves the replacement of oxygen groups by thiol groups, and results in the formation of highly insoluble sulfide minerals (Smedley & Kinniburgh, 2017). The tendency of U and Mo to accumulate in anoxic marine sediments makes them popular proxies for past low oxygen conditions (Bennett & Canfield, 2020; Tribovillard et al., 2006). The decrease in porewater U and Mo concentrations with depth is thus consistent with the observed decrease in SO_4^{2-} concentration (Figures 3d, 5a, and 5b). The sediment content of Mo is consistent with measured porewater depletion because Mo is higher in cores with lower measured porewater concentrations, and an observed gradual increase in the Mo content of the sediment below 5 cm might result from titration of sulfide by the chalcophile Mo (Figures 5a and 5c). Deep sea drilling cores from the northeast Pacific suggest porewater SO_4^{2-} depletions of <7% compared to seawater (Manheim et al., 1970), therefore, the observation that the short cores display quarter to half of the expected S concentration depletion suggests that the sediment depth over which SO_4^{2-} is consumed is not very deep.

A possible explanation for the decrease in SO_4^{2-}, U, Mo and As concentrations with depth in porewaters underlying less productive surface waters is that replenishment rates of oxidants are also lower in these sediments due to their smaller grain size and lower rates of bioturbation compared to sediments found closer to land or in regions

underlying more productive surface waters. An alternative explanation is that the observed drop in concentrations between the overlying water and first porewater sample is a sampling artifact. However, field and laboratory experiments do not suggest Rhizon samplers introduce an error in SO_4^{2-} sampling (James et al., 2021; Steiner et al., 2018). A pressure artifact is also a possibility but the profiles do not change as a function of bottom depths; Mo and U concentrations at Stations 1 and 3 are similar yet Station 3 was almost as deep as Station 2, while Station 1 was shallower and similar in depth to Stations 4 and 5.

The porewater concentration of As increases in the first 2 cm of the sediment and then drops to values lower than the bottom water concentration in cores from Stations 1–3, underlying the subtropical gyre (Figure 4d). Arsenic has two stable oxidation states in seawater, As^{5+} and As^{3+}; however, contrary to other oxyanions, the reduction of As^{5+} to As^{3+} does not involve a large change in the affinity of As to solids (Peterson & Carpenter, 1986). Instead, As is probably removed by adsorption to Fe-oxides (Guénet et al., 2017; Sullivan & Aller, 1996). In Stations 4 and 5, underlying the more productive subpolar gyre, the concentrations of As, Cu and V in the porewater initially remain higher than porewater concentrations from Stations 1–3, underlying the subtropical gyre, and possibly decrease with depth to approach the porewater concentration of the subtropical gyre sediments. This likely represents an enhanced supply of As, Cu, and V when organic matter fluxes to the sediment are higher, and diffusion of these elements to available adsorption or precipitation sites of authigenic minerals. Attenuation of Ni concentrations is faster and might represent a higher affinity to these sediments. The concentration peaks are sharp relative to the sampling resolution, hence a relatively small Station 5 As peak at 1 cm might be a sampling artifact that results from the location of the sampler. It is possible that the coprecipitation of As, Cu and Ni with sulfides, and reduction of V at depths deeper than the core recovered also contribute to the downcore decrease in porewater concentrations (Huerta-Diaz & Morse, 1992; Large et al., 2014). Alternatively, given that the porewater samples were collected above the Mn and Fe oxidation horizon (Figure 3), it is more likely that increased concentrations of metal oxides above the base of the oxic layer adsorb downward diffusing Ni, Cu, As, and V (Hein et al., 2020; Morford & Emerson, 1999; Sullivan & Aller, 1996). Nickel is particularly enriched in diagenetic deep-sea Mn-oxides (Hein et al., 2020), supporting the inference that the presence of Mn-oxides in the sediment contributes to the rapid porewater attenuation of Ni concentrations.

The measured increase in porewater Cr concentration with depth (Figures 6b and 6e) is not expected since the redox transformation of Cr is similar to U and Mo. Chromium is soluble in its oxidized +6 state and tends to form sparingly soluble hydroxides or adsorb to particles in its reduced +3 state (Hassan & Garrison, 1996). The North Pacific red clay porewater Cr profiles are different from a porewater profile from a carbonate-rich sediment core in the Tasman Sea, where Cr concentrations peaked near the surface and decreased below, in correlation with Mn and similar to the behavior of Group I elements in the present study (Janssen et al., 2021). The steep increase in porewater concentration with depth at Station 1 is unique to Cr within this data set, none of the other studied elements show an outstanding depth profile at that station. The source of the higher Station 1 porewater Cr is the Cr-rich sediment (Figure 6h); Hawaii basalts are much higher in Cr concentrations than other sediment sources to the northeast Pacific (Goldberg & Arrhenius, 1958), and the porewater profiles suggest some of this Cr is mobile.

Despite the unusually high flux of porewater Cr from the sampled depth range at Station 1, Cr porewater concentrations at 1 cm below the sediment-water interface at Stations 4 and 5 are similar to the concentration at the same depth at Station 1 (Figure 6e). Cr enrichment in the top cm of the northern stations resembles the profiles of organic matter active elements and suggests a common source. Based on the concentration gradient at the sediment-water interface, sedimentary fluxes of Cr are thus elevated in sediment underlying the productive subpolar gyre, as well as at Station ALOHA near Hawaii, but lower at the northern subtropical gyre Stations 2 and 3. Porewater Cr cycling is commonly thought to be driven by the oxidation of less soluble Cr^{3+} to soluble Cr^{6+} by Mn oxides, a reaction that also shifts Mn to its water soluble form (Janssen et al., 2021; Miletto et al., 2021). In aerobic porewaters, the reduced Mn^{2+} tends to oxidize and precipitate while the oxidized Cr^{6+} remains in solution. An increase in Cr concentrations with depth therefore may reflect the reaction between Cr^{3+} and Mn oxides below the depth range sampled, and upward diffusion of the Cr^{6+} product of this reaction, while the Mn^{2+} is re-oxidized and precipitates at depth. While this mechanism seems to work in some cases, data from this section suggest that reactions with the sediment itself might be more important for Cr than the link to Mn redox chemistry in pelagic clays. In summary, we do not find a correlation between variability of the Cr porewater profiles and eventual fluxes to the bottom water, suggesting that reactions associated with the supply and remineralization of organic matter in the top core control the actual Cr flux across the sediment-water interface.

Barium is unique among the elements studied here because it is not redox sensitive. Instead, porewater barium concentrations are controlled by the saturation of its main mineral form barite ($BaSO_4$), and supply by organic matter (McManus et al., 1998). The deep water of the North Pacific is undersaturated with respect to barite in the subtropical gyre stations; the barite saturation state, calculated using the stoichiometric solubility coefficients from Rushdi et al. (2000), is between 0.8 on the seafloor at Station 2, and ~1 (saturation) on the seafloor at Stations 4 and 5 (Figure 6f). Decomposition of organic matter, and possibly dissolution of some barite and Ba-rich aluminosilicates, increase porewater Ba concentrations in the top centimeters of the sediments. The porewaters approach saturation with respect to barite at Station 2. At Stations 1 and 3, slight supersaturation of barite is reached within the top 5 cm and maintained in the depth range studied (Figure 6f). At Stations 4 and 5, Ba concentrations exceed saturation with respect to barite, and Ba concentrations gradually decrease toward saturation from 5 cm. At most stations, the porewater is still supersaturated at 20 cm depth, the bottom of the studied cores. This suggests that the precipitation of authigenic barite below the sediment-water interface is likely common in red clay sediments; hence, care needs to be taken when interpreting the chemistry of barite impurities for paleoceanographic reconstructions; some of the barite likely forms in the sediments and its composition represents the chemical composition of the porewater and not the productivity of the overlying water column.

Despite this concern about the chemical composition of barite, the bulk sediment Ba concentrations roughly follow the surface water productivity along this transect, supporting the application of the barite accumulation rate as a proxy for paleoproductivity (Figures 1 and 6i). The shape of the Ba porewater profiles raises the possibility that there is a suite of solubility for marine mineral barite, and continuous dissolution of metastable barite in the sediment and precipitation of more stable barite minerals. Support for this notion comes from observations that suggest barite minerals have various strontium contents, which affect the solubility product of barite (Dehairs et al., 1980; Rushdi et al., 2000), and from measurements of Ba ion exchange between the sediment and porewater in multi-corer cores from the equatorial Pacific (Middleton et al., 2023).

4.3. Benthic Fluxes

A key motivation behind this study was to quantify the importance of North Pacific red clay sediments for the oceanic cycle of bio-active elements and thereby complementing benthic flux estimates conducted using water column-based approaches as part of the international GEOTRACES program. The key questions are whether we arrive at similar flux estimates, and what are the causes for disagreements, if present.

We calculate fluxes (J) across the sediment—water interface using Fick's first law of diffusion. This calculation assumes that advection and bio-irrigation are minor relative to molecular diffusion (D_m) in these slowly accumulating deep-sea sediments:

$$J = -\varphi \cdot \frac{D_m}{\theta^2} \cdot \left(\frac{dC}{dZ}\right)_0 \quad (2)$$

Where φ is porosity (Table 1) and $(dC/dZ)_0$ is the concentration gradient across the sediment—bottom-water interface. Molecular diffusion coefficients at 1°C are calculated from Li and Gregory (1974) (Table 3). Tortuosity (θ^2) is calculated using the formulation of Boudreau (1997):

$$\theta^2 = 1 - \ln\left(\varphi^2\right) \quad (3)$$

There are some inaccuracies in the calculations that need to be noted. For most of the studied elements, there are steep concentration gradients between the bottom-water and upper porewater sample. Variable porewater concentrations in the upper parts of the cores leave a large margin of error regarding the peak concentration of the porewater sample and the exact depth of the peak. We assume a diffusive distance of two cm between the effective sampling depth of the first Rhizon and bottom-water and derive dC/dz as a two-point linear slope. The first Rhizon sampler was typically inserted one cm below the sediment-water interface, and we assume that the length of the viscous boundary layer above the sediment-water interface, where internal friction limits water transport, is one cm (Boudreau & Jorgensen, 2001). The porewater was separated in a cold room under a temperature similar to bottom-water conditions, but we do not account for the effect of de-pressurizing on water-solid adsorption equilibrium.

Table 4 presents an extrapolation of the average measured fluxes from the five studied cores to the global aerial extent of deep-sea clay sediment, and the global fluxes of these elements in the river dissolved and particulate

Table 4
Global Fluxes of Trace Elements From Red Clay Sediments and Rivers

		Ba^{2+}	Mn^{2+}	Co^{2+}	Ni^{2+}	Cu^{2+}	CrO_4^{2-}	UO_2^{2+}	$H_2AsO_4^-$	MoO_4^{2-}	VO_4^{2-}	SO_4^{2-}
Global flux from red clay sediment[a]	mol/y	3.9×10^9	3.4×10^8	2.6×10^7	9.6×10^8	4.6×10^9	1.7×10^8	-5.5×10^7	6.1×10^8	-3.6×10^8	6.0×10^9	-1.1×10^{10}
SE	mol/y	3.6×10^9	3.5×10^8	1.3×10^7	8.6×10^8	2.4×10^9	1.1×10^8	2.4×10^7	7.0×10^8	2.6×10^8	2.5×10^9	1.4×10^{10}
River dissolved concentration[b]	nmol/L	440	150	3	9	24	19	1	23	5	20	91,000
River particulate concentration[b]	nmol/g	4,400	19,000	340	1,500	1,600	1,900	13	67	31	3,300	
Freshwater flux[c]	mol/y	2×10^{10}	6×10^9	1×10^8	3×10^8	9×10^8	7×10^8	4×10^7	8×10^8	2×10^8	7×10^8	3×10^{12}
10% Freshwater flux	mol/y		6×10^8	1×10^7	3×10^7	9×10^7	7×10^7					
River particulate flux[c]	mol/y	7×10^{10}	3×10^{11}	5×10^9	2×10^{10}	2×10^{10}	3×10^{10}	2×10^8	1×10^9	5×10^8	5×10^{10}	

[a]Fluxes from red clay sediments were calculated assuming the average of the five studied cores is representative of red clay sediment throughout the oceans, and that red clay sediments cover an area of 1.37×10^8 km^2, 38% of the ocean seafloor. [b]Average river dissolved and particulate concentrations from Martin and Whitfield (1983). [c]Freshwater fluxes were calculated assuming global annual river water discharge of 37,400 km^3. River particulate matter fluxes were calculated assuming rivers carry 1.5×10^{16} g particulate matter to the ocean annually (Martin & Whitfield, 1983).

matter. At least 90% of the dissolved transition metal cations carried by rivers precipitate in the estuarine mixing zone (Martin & Whitfield, 1983); hence, we also calculate the 10% river dissolved flux of these metals. It appears from this comparison that globally fluxes of dissolved trace metals from red clay sediment and rivers are commensurate. The red clay sediment is a larger source of dissolved Ni and Cu to the ocean than rivers. It is important to remember that a substantial part of the material comprising red clay sediment was originally carried to the ocean by rivers, and that the vast majority of ions released from the sediment eventually precipitate again on the sediment, and may repeat this cycle many times until their permanent burial. Calculated fluxes of the oxyanions MoO_4^{2-}, UO_2^{2+}, and SO_4^{2-} into the sediment are too high to be supported by the known inputs of these elements to the ocean and predictions that the main sink for Mo, U and S is anoxic sediment, suggesting these high fluxes are a sampling artifact.

To allow for a more intuitive interpretation of the data, Table 5 displays the concentration addition/removal of dissolved elements from the sediment to the bottom water over a period of 1,000 years. We use this time scale because it is roughly the time it takes Antarctic Bottom Water (AABW) and Lower Circumpolar Deep Water to flow around the North Pacific (DeVries & Primeau, 2011; Matsumoto, 2007). Hence, extrapolating our red clay-based flux measurements to the entire seafloor of the Pacific Ocean, and assuming no removal from the deep-water column, calculated values should coincide with measured changes in water column concentrations between the Southern Ocean region of deep-water formation and the study sites. The calculation also assumes homogenous mixing of a 4,000 m water column.

Comparison of the calculated flux-generated integrated ocean concentration with measured deep ocean concentrations of the studied elements (Table 5) suggests that they can be divided into three groups. The first group includes U, Mo, and SO_4^{2-}. The red clay sediment is a sink for these elements, but this sink is small compared to their seawater concentrations, <1% of their total concentration is removed over a period of 1,000 years. The result is that concentration gradients of U, Mo, and SO_4^{2-} are small compared to their background concentration and their seawater profiles are nearly constant (conservative). It is worth noting that if these fluxes are correct, from an analytical point of view it should be practical to measure the 1%/ka decrease in deep-sea U concentrations suggested for the sediments underlying the subtropical gyre but it is not yet possible to detect the <0.1%/ka decrease in SO_4^{2-} (Table 5).

The second group includes elements for which the sediment is an important source but not the main source to the intermediate and deep ocean water column. This group includes Ba, Ni, Cr, and As. Fluxes from the sediment explain 5%–20% of the water column variability of these elements. Water column profiles of Ba, Ni, Cr, and As generally show peak concentrations at intermediate water depths rather than near the bottom, confirming that most re-mineralization takes place in the water column (Andreae, 1979; Chan et al., 1976; Moos & Boyle, 2019; Zheng et al., 2021). The structure of the water column profiles reflects a combination of vertical export and remineralization and horizontal transport of water masses with different initial trace metal concentrations (Vance et al., 2017).

Our calculations suggest particularly high benthic Ba fluxes at Station 4. This result is in accord with water column measurements of Ba concentrations from GEOTRACES section GP15, which suggest that the highest Ba concentrations along the GP15 section are found in the deep-water at locations adjacent to our Station 4 (GEOTRACES Intermediate Data Product Group, 2021, 2023).

The third group includes the elements Mn, Co, Fe, and Cu, for which the sediment is the main source to the deep ocean. The sedimentary source of these elements often exceeds deep-water concentrations, indicating that an important fraction does not remain in the dissolved pool; this is consistent with the short residence time of these elements in the ocean (Table 5; Horner et al., 2021; Zheng et al., 2019, 2021). The high abundance of Mn-Fe nodules and crusts on the Pacific seafloor serves as evidence for the oxidation and removal of Fe and Mn from the water column, and these nodules can adsorb other elements, including Co, Cu, and Ni (Shaw et al., 1990). Based on the sedimentary Mn fluxes (Tables 4 and 5) and the Pacific Ocean distribution of dissolved and labile particulate Mn (Zheng et al., 2019, 2022), it is suggested that Mn is

Table 5
Contribution of Benthic Diffusive Fluxes to the Water Column Concentration of the Studied Elements Over a Period of 1,000 Years, Assuming Complete Mixing of a 4,000 m Deep Water Column

	Ba^{2+} (nmol kg^{-1} ka^{-1})	Mn^{2+} (nmol kg^{-1} ka^{-1})	Co^{2+} (pmol kg^{-1} ka^{-1})	Ni^{2+} (nmol kg^{-1} ka^{-1})	Cu^{2+} (nmol kg^{-1} ka^{-1})	CrO_4^{2-} (nmol kg^{-1} ka^{-1})	UO_2^{2+} (nmol kg^{-1} ka^{-1})	$H_2AsO_4^-$ (nmol kg^{-1} ka^{-1})	MoO_4^{2-} (nmol kg^{-1} ka^{-1})	VO_4^{2-} (nmol kg^{-1} ka^{-1})	SO_4^{2-} (μmol kg^{-1} ka^{-1})
Station 1	1.8	0.01	49	1.0	10	0.31	−0.11	1.9	−0.68	17	−8
Station 2	−0.8	0.19	28	0.3	3.2	0.08	−0.16	0.1	−1.7	6	−52
Station 3	6.1	0.05	29	0.3	2.5	0.11	−0.13	−0.5	−0.74	5	−5
Station 4	23	1.1	22	5.5	13	0.77	−0.07	3.4	0.07	15	−48
Station 5	4.3	1.6	100	1.3	12	0.25	−0.02	0.5	−0.21	12	17
Average	6.8	0.60	46	1.7	8.1	0.30	−0.10	1.1	−0.64	11	−19
SE	6.4	0.62	23	1.5	4.2	0.19	0.04	1.2	0.46	4	25
Global seawater range	33.2–131.1[a]	0.12–4.1[a]	15–157[a]	2.1–9.3[a]	0.38–3.8[a]	2–6[b]	11.9–13.1[a]	10–22[c]	105–143[a]	22.9–35.3[a]	28,200[d]
Residence time estimate (ka)	3.5–21[e]	1.3[f]	0.3[f]	10–30[g]	2–5[g]	6[g]	500[f]	39[f]	440[g]	100[h]	10,000[d]

[a]The global seawater range of Ba, Mn, Co, Ni, Cu, U, Mo, and V are the 5 and 95 percentiles of all bottle dissolved concentrations in the GEOTRACES intermediate data product (2021). The actual open ocean range of Mo concentrations is much narrower than suggested from this calculation (Horner et al., 2021). Seawater concentration units are nmol kg^{-1}, except Co (pmol kg^{-1}) and SO_4^{2-} (μmol kg^{-1}). [b]Cr concentration range from Horner et al. (2021). [c]Seawater As concentration range from Cutter and Cutter (2006) and Wurl et al. (2015). [d]Concentration and residence time estimate of sulfate from Tagliabue (2019) at practical salinity of 35. [e]Residence time estimates for Ba vary. It is 7–21 ka according to Horner and Crockford (2021) but 3.5–5 ka according to Rahman et al. (2022). [f]Residence time estimates for Mn, Co, U, and As are from Broecker and Peng (1982). [g]Residence time estimates for Ni, Cu, Cr, and Mo are from Horner et al. (2021) and references therein. [h]Residence time estimate for V from Shiller and Boyle (1987).

diffusing from the sediment to the bottom water, where it forms labile particulates that accumulate on top of the sediment. Settling of Mn oxides from the upper ocean is another source of particulate Mn to the top sediments, which might be the dominant one. The accretion of Mn nodules thus appears to be largely fed from above.

The average Cu fluxes we calculated, 92 ± 48 nmol m^{-2} d^{-1} are within range but slightly higher than Cu fluxes reported for east Pacific subtropical and equatorial red clays by Sawlan and Murray (1983), 77 nmol m^{-2} d^{-1}, and Klinkhammer (1980), 49 nmol m^{-2} d^{-1}. Our values are also higher than but within uncertainty equal to calculations of the benthic flux required to balance the Pacific Cu profiles by Boyle et al. (1977) with a value of 68 nmol m^{-2} d^{-1}. Our calculated Cu flux is driven upwards by the high Cu fluxes from sediments underlying the productive waters of the subpolar gyre. The subtropical gyre is larger than the subpolar gyre, and deep water has a longer exposure time to sediments underlying the subtropical gyre; hence, the average Pacific Cu flux is probably slightly lower than our mean calculated flux (which is not area-averaged), which is in good agreement with previous studies. The same conclusion is likely applicable to Ni and Mn fluxes, which are also much higher in sediments underlying the subpolar gyre.

Vanadium is the one element that appears unusual in this group. The porewater profiles suggest an extremely active cycle, and the resulting calculated fluxes of V to the bottom water are very high (Figure 4a and Table 4). Scaled up to the area of the red clay covered global seafloor (1.4×10^{14} m^2) our measurements suggest a V flux of 6×10^9 mol yr^{-1}. The main sinks for dissolved V in the deep ocean are hydrothermal vents, consuming ~5×10^8 mol V yr^{-1} (Schlesinger et al., 2017). This is inconsistent with observations that water column profiles of V are semi-conservative (Collier, 1984; Ho et al., 2018; Jeandel et al., 1987). This observation is not unique to the present study, similar results were reported for other sites in the Pacific and Atlantic Oceans (Emerson & Huested, 1991; Heggie et al., 1986).

The chemical behavior of V strongly depends on its redox chemistry. In oxygenated waters, V is found in its +5 oxidation state and the majority of V is in the form of the highly water-soluble vanadate ions ($H_2VO_4^-$ and HVO_4^{2-}); under mildly reducing conditions, V is reduced to the +4 oxidation state, mostly as the particle reactive vanadyl (VO^{2+}) ion (Huang et al., 2015; Wehrli & Stumm, 1989). As a solution to the apparent discrepancy between high porewater V concentrations and lower actual apparent fluxes of V from the sediment, Heggie et al. (1986) and Emerson and Huested (1991) suggested that the high affinity of vanadyl to dissolved OC may

result in greatly retarded diffusion coefficients and lower fluxes to the bottom water. This solution does not explain V retention in aerobic pelagic clays since the redox conditions suggest that it should be found in its V^{5+} oxidation state. In the present study, porewater V concentrations are much higher in sediments underlying the more productive subpolar gyre stations, suggesting that V delivery to the sediment is associated with organic matter (Figure 4a). Under aerobic conditions, vanadates tend to adsorb to Fe oxides (Auger et al., 1999; Wehrli & Stumm, 1989; Wu et al., 2020, 2022). Adsorption of V diffusing out of the sediment to Fe oxides can remove the excess from the water column, for example, in bottom nepheloid layers. The persistently high porewater V concentrations suggest that at least part of the V adsorption to Fe oxides is reversible; the active V fraction is adsorbed and released many times leading to lower than calculated fluxes from the sediment to the bottom water.

5. Implications

The main finding of this study is that trace element concentrations vary by up to an order-of-magnitude under aerobic conditions in porewaters of the top 10 cm of the sediment column. The nature and quantity of material falling on the seabed, resulting microbial activity, and the vastly different physical environment in the sediment and bottom water can produce large concentration variability without requiring significant changes in redox conditions. This implies that calculations of benthic fluxes from cores retrieved using any method that fails to collect undisturbed surface sediment produce incorrect results. On the other hand, the porewater extracted from aerobic sediments with undisturbed surfaces produces reasonable benthic fluxes that are in good agreement with the water column concentration variability of most elements.

The fact that redox conditions in the top red clay sediment are similar to bottom water redox conditions in the abyssal ocean thus removes a major factor of uncertainty. Pelagic red clay sediment represents almost 40% of the global ocean seafloor. The finding that trace metal fluxes from red clay sediment scale to predictions from the global water column distribution of these elements suggests that even though porewaters of sediment from shallower depths display larger concentration variability of many elements because of the variable redox conditions, this does not necessarily translate to long-range transport of these metals. The reason is that the re-oxidation of reduced Mn and Fe in the continental shelf top sediment and bottom water scavenges other trace metals and limits their transport. The outcome is that on the global scale, element fluxes per unit area from aerobic sediment might be as important as fluxes from reducing sediment in maintaining the chemical composition of the ocean. Given the vast aerial distribution of red clay sediment, this highlights its importance in global element cycles.

Paleoceanographic investigations use many of the elements studied here for the interpretation of past ocean conditions based on their bulk sediment concentrations. For example, combinations of U, Mo, and V concentration data are suggested to inform past redox conditions, and variability in the accumulation rates of Ba, Ni, and Cu may inform past productivity (Bennett & Canfield, 2020; Böning et al., 2015; Dymond et al., 1992; Steiner et al., 2017; Tribovillard et al., 2006). The porewater data provide direct indications that mobility of these elements is expected under aerobic conditions; part of the fraction eventually buried diffuses down from the surface to deeper sediment. This is the case both for the redox-sensitive elements and for elements with affinity to organic matter. The downward diffusion adds a degree of uncertainty regarding the timing and magnitude of changes recorded in the sediment; however, for most elements this is a minor complication because only a small fraction of the solid phase sediment is mobile, and the mobile fraction normally precipitates a few cm deeper, which might be on the same length-scale as bioturbation. The sediment profiles are still prone to diagenetic alteration below the 12 cm studied here, but for a proxy to genuinely represent past water-column conditions, they must already be recorded in the top sediment. We find that the sediment content of these elements does not necessarily represent changes in productivity or redox conditions. This is particularly obvious for Ni in this study, where the sediment content is lowest in the productive subpolar Station 5 and highest in the oligotrophic subtropical Stations 1 and 2, yet variability is observed for all studied elements.

Data Availability Statement

Porewater data generated in this study are available at Steiner et al. (2022c) https://doi.pangaea.de/10.1594/PANGAEA.946881. Sediment data were submitted to Pangaea and are available as supporting online information.

Acknowledgments
The cruise on-board RV Kilo Moana was funded by NSF Ocean Acidification Grant OCE1220600. We thank Nick Rollins, Sijia Dong and Abby Lunstrum for analyzing sediment OC content and porosity. We thank Dalton Hardisty and an anonymous reviewer for their constructive comments that helped improve the manuscript. Open Access funding enabled and organized by Projekt DEAL.

References

Algeo, T. J., & Liu, J. (2020). A re-assessment of elemental proxies for paleoredox analysis. *Chemical Geology*, *540*, 119549. https://doi.org/10.1016/j.chemgeo.2020.119549

Anderson, R. F. (2020). GEOTRACES: Accelerating research on the marine biogeochemical cycles of trace elements and their isotopes. *Annual Review of Marine Science*, *12*(1), 49–85. https://doi.org/10.1146/annurev-marine-010318-095123

Andreae, M. O. (1979). Arsenic speciation in seawater and interstitial waters: The influence of biological-chemical interactions on the chemistry of a trace element. *Limnology & Oceanography*, *24*(3), 440–452. https://doi.org/10.4319/lo.1979.24.3.0440

Andrews, E., Pogge von Strandmann, P. A. E., & Fantle, M. S. (2020). Exploring the importance of authigenic clay formation in the global Li cycle. *Geochimica et Cosmochimica Acta*, *289*, 47–68. https://doi.org/10.1016/j.gca.2020.08.018

Arndt, S., Jorgensen, B. B., LaRowe, D. E., Middelburg, J. J., Pancost, R. D., & Regnier, P. (2013). Quantifying the degradation of organic matter in marine sediments: A review and synthesis. *Earth-Science Reviews*, *123*, 53–86. https://doi.org/10.1016/j.earscirev.2013.02.008

Auger, Y., Bodineau, L., Leclercq, S., & Wartel, M. (1999). Some aspects of vanadium and chromium chemistry in the English Channel. *Continental Shelf Research*, *19*(15–16), 2003–2018. https://doi.org/10.1016/s0278-4343(99)00050-3

Ayers, J. M., & Lozier, M. S. (2010). Physical controls on the seasonal migration of the North Pacific transition zone chlorophyll front. *Journal of Geophysical Research*, *115*(C5), C05001. https://doi.org/10.1029/2009jc005596

Bargar, J. R., Williams, K. H., Campbell, K. M., Long, P. E., Stubbs, J. E., Suvorova, E. I., et al. (2013). Uranium redox transition pathways in acetate-amended sediments. *Proceedings of the National Academy of Sciences of the United States of America*, *110*(12), 4506–4511. https://doi.org/10.1073/pnas.1219198110

Bennett, W. W., & Canfield, D. E. (2020). Redox-sensitive trace metals as paleoredox proxies: A review and analysis of data from modern sediments. *Earth-Science Reviews*, *204*, 103175. https://doi.org/10.1016/j.earscirev.2020.103175

Berger, W. H., Adelseck, C. G., Jr., & Mayer, L. A. (1976). Distribution of carbonate in surface sediments of the Pacific Ocean. *Journal of Geophysical Research*, *81*(15), 2617–2627. https://doi.org/10.1029/jc081i015p02617

Berner, R. A. (1980). *Early diagenesis: A theoretical approach*. Princeton University Press.

Böning, P., Shaw, T., Pahnke, K., & Brumsack, H. J. (2015). Nickel as indicator of fresh organic matter in upwelling sediments. *Geochimica et Cosmochimica Acta*, *162*, 99–108. https://doi.org/10.1016/j.gca.2015.04.027

Boudreau, B. P. (1997). *Diagenetic models and their implementation*. Springer.

Boudreau, B. P., & Jorgensen, B. B. (2001). *The benthic boundary layer: Transport processes and biogeochemistry*. Oxford University Press.

Boudreau, B. P., Sulpis, O., & Mucci, A. (2020). Control of $CaCO_3$ dissolution at the deep seafloor and its consequences. *Geochimica et Cosmochimica Acta*, *268*, 90–106. https://doi.org/10.1016/j.gca.2019.09.037

Boyd, P. W., Ellwood, M. J., Tagliabue, A., & Twining, B. S. (2017). Biotic and abiotic retention, recycling and remineralization of metals in the ocean. *Nature Geoscience*, *10*(3), 167–173. https://doi.org/10.1038/ngeo2876

Boyle, E. A., Sclater, F. R., & Edmond, J. M. (1977). The distribution of dissolved copper in the Pacific. *Earth and Planetary Science Letters*, *37*(1), 38–54. https://doi.org/10.1016/0012-821x(77)90144-3

Broecker, W. S., & Peng, T.-H. (1982). *Tracers in the sea*. The Lamont-Doherty Geological Observatory.

Bruland, K. W. (1980). Oceanographic distributions of cadmium, zinc, nickel, and copper in the North Pacific. *Earth and Planetary Science Letters*, *47*(2), 176–198. https://doi.org/10.1016/0012-821x(80)90035-7

Burdige, D. J. (2006). *Geochemistry of marine sediments*. Princeton University Press.

Burton, J. D. (1996). The ocean: A global chemical system. In C. P. Summerhayes & S. A. Thorpe (Eds.), *Oceanography: An illustrated guide* (pp. 165–181). Manson.

Calvert, S. E., & Pedersen, T. F. (1993). Geochemistry of recent oxic and anoxic marine sediments: Implications for the geological record. *Marine Geology*, *113*(1–2), 67–88. https://doi.org/10.1016/0025-3227(93)90150-t

Cameron, V., & Vance, D. (2014). Heavy nickel isotope compositions in rivers and the oceans. *Geochimica et Cosmochimica Acta*, *128*, 195–211. https://doi.org/10.1016/j.gca.2013.12.007

Chan, L. H., Edmond, J. M., Stallard, R. F., Broecker, W. S., Chung, Y. C., Weiss, R. F., & Ku, T. L. (1976). Radium and barium at GEOSECS stations in the Atlantic and Pacific. *Earth and Planetary Science Letters*, *32*(2), 258–267. https://doi.org/10.1016/0012-821x(76)90066-2

Chen, C., Feely, R., & Gendron, J. (1988). Lysocline, calcium carbonate compensation depth, and calcareous sediments in the North Pacific Ocean. *Pacific Science*, *42*, 237–252.

Chmiel, R., Lanning, N., Laubach, A., Lee, J. M., Fitzsimmons, J., Hatta, M., et al. (2022). Major processes of the dissolved cobalt cycle in the North and equatorial Pacific Ocean. *Biogeosciences*, *19*(9), 2365–2395. https://doi.org/10.5194/bg-19-2365-2022

Cochran, J. K., Carey, A. E., Sholkovitz, E. R., & Surprenant, L. D. (1986). The geochemistry of uranium and thorium in coastal marine sediments and sediment pore waters. *Geochimica et Cosmochimica Acta*, *50*(5), 663–680. https://doi.org/10.1016/0016-7037(86)90344-3

Collier, R. W. (1984). Particulate and dissolved vanadium in the North Pacific Ocean. *Nature*, *309*(5967), 441–444. https://doi.org/10.1038/309441a0

Crusius, J., Calvert, S., Pedersen, T., & Sage, D. (1996). Rhenium and molybdenum enrichments in sediments as indicators of oxic, suboxic and sulfidic conditions of deposition. *Earth and Planetary Science Letters*, *145*(1–4), 65–78. https://doi.org/10.1016/s0012-821x(96)00204-x

Cutter, G. A., & Cutter, L. S. (2006). Biogeochemistry of arsenic and antimony in the North Pacific Ocean. *Geochemistry, Geophysics, Geosystems*, *7*(5), Q05M08. https://doi.org/10.1029/2005gc001159

Dehairs, F., Chesselet, R., & Jedwab, J. (1980). Discrete suspended particles of barite and the barium cycle in the open ocean. *Earth and Planetary Science Letters*, *49*(2), 528–550. https://doi.org/10.1016/0012-821x(80)90094-1

DeVries, T., & Primeau, F. (2011). Dynamically and observationally constrained estimates of water-mass distributions and ages in the global ocean. *Journal of Physical Oceanography*, *41*(12), 2381–2401. https://doi.org/10.1175/jpo-d-10-05011.1

D'Hondt, S., Inagaki, F., Zarikian, C. A., Abrams, L. J., Dubois, N., Engelhardt, T., et al. (2015). Presence of oxygen and aerobic communities from sea floor to basement in deep-sea sediments. *Nature Geoscience*, *8*(4), 299–304. https://doi.org/10.1038/ngeo2387

Diesing, M. (2020). Deep-sea sediments of the global ocean. *Earth System Science Data*, *12*(4), 3367–3381. https://doi.org/10.5194/essd-12-3367-2020

Dong, S., Berelson, W. M., Rollins, N. E., Subhas, A. V., Naviaux, J. D., Celestian, A. J., et al. (2019). Aragonite dissolution kinetics and calcite/aragonite ratios in sinking and suspended particles in the North Pacific. *Earth and Planetary Science Letters*, *515*, 1–12. https://doi.org/10.1016/j.epsl.2019.03.016

Dong, S., Wang, X. T., Subhas, A. V., Pavia, F. J., Adkins, J. F., & Berelson, W. M. (2022). Depth profiles of suspended carbon and nitrogen along a North Pacific transect: Concentrations, isotopes, and ratios. *Limnology & Oceanography*, *67*(1), 247–260. https://doi.org/10.1002/lno.11989

Dunlea, A. G., Murray, R. W., Ramos, D. P. S., & Higgins, J. A. (2017). Cenozoic global cooling and increased seawater Mg/Ca via reduced reverse weathering. *Nature Communications*, *8*(1), 844. https://doi.org/10.1038/s41467-017-00853-5

Dutkiewicz, A., Müller, R. D., O'Callaghan, S., & Jónasson, H. (2015). Census of seafloor sediments in the world's ocean. *Geology*, *43*(9), 795–798. https://doi.org/10.1130/g36883.1

Dymond, J., Suess, E., & Lyle, M. (1992). Barium in deep-sea sediment: A geochemical proxy for paleoproductivity. *Paleoceanography*, *7*(2), 163–181. https://doi.org/10.1029/92pa00181

Emerson, S. R., & Huested, S. S. (1991). Ocean anoxia and the concentrations of molybdenum and vanadium in seawater. *Marine Chemistry*, *34*(3–4), 177–196. https://doi.org/10.1016/0304-4203(91)90002-e

Fantle, M. S., & DePaolo, D. J. (2007). Ca isotopes in carbonate sediment and pore fluid from ODP Site 807A: The Ca^{2+}(aq)-calcite equilibrium fractionation factor and calcite recrystallization rates in Pleistocene sediments. *Geochimica et Cosmochimica Acta*, *71*(10), 2524–2546. https://doi.org/10.1016/j.gca.2007.03.006

Froelich, P. N., Klinkhammer, G. P., Bender, M. L., Luedtke, N. A., Heath, G. R., Cullen, D., et al. (1979). Early oxidation of organic matter in pelagic sediments of the eastern equatorial Atlantic: Suboxic diagenesis. *Geochimica et Cosmochimica Acta*, *43*(7), 1075–1090. https://doi.org/10.1016/0016-7037(79)90095-4

GEOTRACES Intermediate Data Product Group. (2021). *The GEOTRACES intermediate data product 2021 (IDP2021)*. NERC EDS British Oceanographic Data Centre NOC.

GEOTRACES Intermediate Data Product Group. (2023). *The GEOTRACES intermediate data product 2021 version 2 (IDP2021v2)*. NERC EDS British Oceanographic Data Centre NOC.

Glasby, G. P. (1991). Mineralogy, geochemistry, and origin of Pacific red clays: A review. *New Zealand Journal of Geology and Geophysics*, *34*(2), 167–176. https://doi.org/10.1080/00288306.1991.9514454

Goldberg, E. D., & Arrhenius, G. O. S. (1958). Chemistry of Pacific pelagic sediments. *Geochimica et Cosmochimica Acta*, *13*(2–3), 153–212. https://doi.org/10.1016/0016-7037(58)90046-2

Guénet, H., Davranche, M., Vantelon, D., Bouhnik-Le Coz, M., Jardé, E., Pierson-Wickmann, A.-C., et al. (2017). Highlighting the wide variability in arsenic speciation in wetlands: A new insight into the control of the behavior of arsenic. *Geochimica et Cosmochimica Acta*, *203*, 284–302. https://doi.org/10.1016/j.gca.2017.01.013

Hassan, S. M., & Garrison, A. W. (1996). Distribution of chromium species between soil and porewater. *Chemical Speciation and Bioavailability*, *8*(3–4), 85–103. https://doi.org/10.1080/09542299.1996.11083273

Hawco, N. J., Lam, P. J., Lee, J.-M., Ohnemus, D. C., Noble, A. E., Wyatt, N. J., et al. (2018). Cobalt scavenging in the mesopelagic ocean and its influence on global mass balance: Synthesizing water column and sedimentary fluxes. *Marine Chemistry*, *201*, 151–166. https://doi.org/10.1016/j.marchem.2017.09.001

Hayes, C. T., Black, E. E., Anderson, R. F., Baskaran, M., Buesseler, K. O., Charette, M. A., et al. (2018). Flux of particulate elements in the North Atlantic Ocean constrained by multiple radionuclides. *Global Biogeochemical Cycles*, *32*(12), 1738–1758. https://doi.org/10.1029/2018gb005994

Heggie, D., Kahn, D., & Fischer, K. (1986). Trace metals in metalliferous sediments, MANOP site M: Interfacial pore water profiles. *Earth and Planetary Science Letters*, *80*(1–2), 106–116. https://doi.org/10.1016/0012-821x(86)90023-3

Heggie, D., & Lewis, T. (1984). Cobalt in pore waters of marine sediments. *Nature*, *311*(5985), 453–455. https://doi.org/10.1038/311453a0

Hein, J. R., Koschinsky, A., & Kuhn, T. (2020). Deep-ocean polymetallic nodules as a resource for critical materials. *Nature Reviews Earth & Environment*, *1*(3), 158–169. https://doi.org/10.1038/s43017-020-0027-0

Hein, J. R., Yeh, H.-W., & Alexander, E. (1979). Origin of iron-rich montmorillonite from the manganese nodule belt of the North Equatorial Pacific. *Clays and Clay Minerals*, *27*(3), 185–194. https://doi.org/10.1346/ccmn.1979.0270303

Ho, P., Lee, J.-M., Heller, M. I., Lam, P. J., & Shiller, A. M. (2018). The distribution of dissolved and particulate Mo and V along the US GEOTRACES East Pacific Zonal Transect (GP16): The roles of oxides and biogenic particles in their distributions in the oxygen deficient zone and the hydrothermal plume. *Marine Chemistry*, *201*, 242–255. https://doi.org/10.1016/j.marchem.2017.12.003

Ho, T.-Y., Quigg, A., Finkel, Z. V., Milligan, A. J., Wyman, K., Falkowski, P. G., & Morel, F. M. M. (2003). The elemental composition of some marine phytoplankton. *Journal of Phycology*, *39*(6), 1145–1159. https://doi.org/10.1111/j.0022-3646.2003.03-090.x

Homoky, W. B., Weber, T., Berelson, W. M., Conway, T. M., Henderson, G. M., van Hulten, M., et al. (2016). Quantifying trace element and isotope fluxes at the ocean-sediment boundary: A review. *Philosophical Transactions of the Royal Society A: Mathematical, Physical & Engineering Sciences*, *374*(2081), 20160246. https://doi.org/10.1098/rsta.2016.0246

Horner, T. J., & Crockford, P. W. (2021). *Barium isotopes: Drivers, dependencies, and distributions through space and time*. Cambridge University Press.

Horner, T. J., Kinsley, C. W., & Nielsen, S. G. (2015). Barium-isotopic fractionation in seawater mediated by barite cycling and oceanic circulation. *Earth and Planetary Science Letters*, *430*, 511–522. https://doi.org/10.1016/j.epsl.2015.07.027

Horner, T. J., Little, S. H., Conway, T. M., Farmer, J. R., Hertzberg, J. E., Janssen, D. J., et al. (2021). Bioactive trace metals and their isotopes as paleoproductivity proxies: An assessment using GEOTRACES-era data. *Global Biogeochemical Cycles*, *35*(11), e2020GB006814. https://doi.org/10.1029/2020gb006814

Hou, Y., Hammond, D. E., Berelson, W. M., Kemnitz, N., Adkins, J. F., & Lunstrum, A. (2019). Spatial patterns of benthic silica flux in the North Pacific reflect upper ocean production. *Deep Sea Research Part I: Oceanographic Research Papers*, *148*, 25–33. https://doi.org/10.1016/j.dsr.2019.04.013

Huang, J.-H., Huang, F., Evans, L., & Glasauer, S. (2015). Vanadium: Global (bio)geochemistry. *Chemical Geology*, *417*, 68–89. https://doi.org/10.1016/j.chemgeo.2015.09.019

Huerta-Diaz, M. A., & Morse, J. W. (1992). Pyritization of trace metals in anoxic marine sediments. *Geochimica et Cosmochimica Acta*, *56*(7), 2681–2702. https://doi.org/10.1016/0016-7037(92)90353-k

James, D. H., Bradbury, H. J., Antler, G., Steiner, Z., Hutchings, A. M., Sun, X., et al. (2021). Assessing sedimentary boundary layer calcium carbonate precipitation and dissolution using the calcium isotopic composition of pore fluids. *Frontiers in Earth Science*, *9*, 587085. https://doi.org/10.3389/feart.2021.601194

Janssen, D. J., Rickli, J., Abbott, A. N., Ellwood, M. J., Twining, B. S., Ohnemus, D. C., et al. (2021). Release from biogenic particles, benthic fluxes, and deep water circulation control Cr and δ^{53}Cr distributions in the ocean interior. *Earth and Planetary Science Letters*, *574*, 117163. https://doi.org/10.1016/j.epsl.2021.117163

Jeandel, C., Caisso, M., & Minster, J. (1987). Vanadium behaviour in the global ocean and in the Mediterranean Sea. *Marine Chemistry*, *21*(1), 51–74. https://doi.org/10.1016/0304-4203(87)90029-6

Kellogg, R. M., McIlvin, M. R., Vedamati, J., Twining, B. S., Moffett, J. W., Marchetti, A., et al. (2020). Efficient zinc/cobalt inter-replacement in northeast Pacific diatoms and relationship to high surface dissolved Co: Zn ratios. *Limnology & Oceanography*, *65*(11), 2557–2582. https://doi.org/10.1002/lno.11471

Kemnitz, N., Hammond, D. E., Henderson, P., Le Roy, E., Charette, M., Moore, W., et al. (2022). Actinium and radium fluxes from the seabed in the northeast Pacific Basin. *Marine Chemistry*, *250*, 104180. https://doi.org/10.1016/j.marchem.2022.104180
Klinkhammer, G., Heggie, D. T., & Graham, D. W. (1982). Metal diagenesis in oxic marine sediments. *Earth and Planetary Science Letters*, *61*(2), 211–219. https://doi.org/10.1016/0012-821x(82)90054-1
Klinkhammer, G. P. (1980). Early diagenesis in sediments from the eastern equatorial Pacific, II. Pore water metal results. *Earth and Planetary Science Letters*, *49*(1), 81–101. https://doi.org/10.1016/0012-821x(80)90151-x
Large, R. R., Halpin, J. A., Danyushevsky, L. V., Maslennikov, V. V., Bull, S. W., Long, J. A., et al. (2014). Trace element content of sedimentary pyrite as a new proxy for deep-time ocean–atmosphere evolution. *Earth and Planetary Science Letters*, *389*, 209–220. https://doi.org/10.1016/j.epsl.2013.12.020
Li, Y. H., & Gregory, S. (1974). Diffusion of ions in sea water and in deep-sea sediments. *Geochimica et Cosmochimica Acta*, *38*(5), 703–714. https://doi.org/10.1016/0016-7037(74)90145-8
Little, S. H., Vance, D., Lyons, T. W., & McManus, J. (2015). Controls on trace metal authigenic enrichment in reducing sediments: Insights from modern oxygen-deficient settings. *American Journal of Science*, *315*(2), 77–119. https://doi.org/10.2475/02.2015.01
Manheim, F., Chan, K., & Sayles, F. (1970). Interstitial water studies on small core samples, Deep Sea Drilling Project. *Leg 5. Initial Reports of the Deep Sea Drilling Project*, *5*, 501–511.
Martin, J.-M., & Whitfield, M. (1983). The significance of the river input of chemical elements to the ocean. In C. S. Wong, E. Boyle, K. W. Bruland, J. D. Burton, & E. D. Goldberg (Eds.), *Trace metals in sea water* (pp. 265–296). Springer US.
Martinez-Ruiz, F., Paytan, A., Gonzalez-Muñoz, M. T., Jroundi, F., Abad, M. M., Lam, P. J., et al. (2019). Barite formation in the ocean: Origin of amorphous and crystalline precipitates. *Chemical Geology*, *511*, 441–451. https://doi.org/10.1016/j.chemgeo.2018.09.011
Matsumoto, K. (2007). Radiocarbon-based circulation age of the world oceans. *Journal of Geophysical Research*, *112*(C9), C09004. https://doi.org/10.1029/2007jc004095
McManus, J., Berelson, W. M., Klinkhammer, G. P., Johnson, K. S., Coale, K. H., Anderson, R. F., et al. (1998). Geochemistry of barium in marine sediments: Implications for its use as a paleoproxy. *Geochimica et Cosmochimica Acta*, *62*(21–22), 3453–3473. https://doi.org/10.1016/s0016-7037(98)00248-8
Middleton, J. T., Paytan, A., Auro, M., Saito, M. A., & Horner, T. J. (2023). Barium isotope signatures of barite–fluid ion exchange in Equatorial Pacific sediments. *Earth and Planetary Science Letters*, *612*, 118150. https://doi.org/10.1016/j.epsl.2023.118150
Miletto, M., Wang, X., Planavsky, N. J., Luther, G. W., Lyons, T. W., & Tebo, B. M. (2021). Marine microbial Mn(II) oxidation mediates Cr(III) oxidation and isotope fractionation. *Geochimica et Cosmochimica Acta*, *297*, 101–119. https://doi.org/10.1016/j.gca.2021.01.008
Moffett, J. W., & Ho, J. (1996). Oxidation of cobalt and manganese in seawater via a common microbially catalyzed pathway. *Geochimica et Cosmochimica Acta*, *60*(18), 3415–3424. https://doi.org/10.1016/0016-7037(96)00176-7
Moos, S. B., & Boyle, E. A. (2019). Determination of accurate and precise chromium isotope ratios in seawater samples by MC-ICP-MS illustrated by analysis of SAFe Station in the North Pacific Ocean. *Chemical Geology*, *511*, 481–493. https://doi.org/10.1016/j.chemgeo.2018.07.027
Morford, J. L., & Emerson, S. (1999). The geochemistry of redox sensitive trace metals in sediments. *Geochimica et Cosmochimica Acta*, *63*(11–12), 1735–1750. https://doi.org/10.1016/s0016-7037(99)00126-x
Morford, J. L., Emerson, S. R., Breckel, E. J., & Kim, S. H. (2005). Diagenesis of oxyanions (V, U, Re, and Mo) in pore waters and sediments from a continental margin. *Geochimica et Cosmochimica Acta*, *69*(21), 5021–5032. https://doi.org/10.1016/j.gca.2005.05.015
Murray, J. W., & Grundmanis, V. (1980). Oxygen consumption in pelagic marine sediments. *Science*, *209*(4464), 1527–1530. https://doi.org/10.1126/science.209.4464.1527
Parkes, R. J., Cragg, B. A., Bale, S. J., Getlifff, J. M., Goodman, K., Rochelle, P. A., et al. (1994). Deep bacterial biosphere in Pacific Ocean sediments. *Nature*, *371*(6496), 410–413. https://doi.org/10.1038/371410a0
Peterson, M. L., & Carpenter, R. (1986). Arsenic distributions in porewaters and sediments of Puget Sound, Lake Washington, the Washington coast and Saanich Inlet, B.C. *Geochimica et Cosmochimica Acta*, *50*(3), 353–369. https://doi.org/10.1016/0016-7037(86)90189-4
Rahman, S., Shiller, A. M., Anderson, R. F., Charette, M. A., Hayes, C. T., Gilbert, M., et al. (2022). Dissolved and particulate barium distributions along the US GEOTRACES North Atlantic and East Pacific zonal transects (GA03 and GP16): Global implications for the marine barium cycle. *Global Biogeochemical Cycles*, *36*(6), e2022GB007330. https://doi.org/10.1029/2022gb007330
Roshan, S., DeVries, T., & Wu, J. (2020). Constraining the global ocean Cu cycle with a data-assimilated diagnostic model. *Global Biogeochemical Cycles*, *34*(11), e2020GB006741. https://doi.org/10.1029/2020gb006741
Rudnick, R. L., & Gao, S. (2003). 3.01—Composition of the continental crust. In H. D. Holland & K. K. Turekian (Eds.), *Treatise on geochemistry* (pp. 1–64). Pergamon. https://doi.org/10.1016/B0-08-043751-6/03016-4
Rushdi, A. I., McManus, J., & Collier, R. W. (2000). Marine barite and celestite saturation in seawater. *Marine Chemistry*, *69*(1–2), 19–31. https://doi.org/10.1016/s0304-4203(99)00089-4
Saito, M. A., Goepfert, T. J., Noble, A. E., Bertrand, E. M., Sedwick, P. N., & DiTullio, G. R. (2010). A seasonal study of dissolved cobalt in the Ross Sea, Antarctica: Micronutrient behavior, absence of scavenging, and relationships with Zn, Cd, and P. *Biogeosciences*, *7*(12), 4059–4082. https://doi.org/10.5194/bg-7-4059-2010
Sawlan, J. J., & Murray, J. W. (1983). Trace metal remobilization in the interstitial waters of red clay and hemipelagic marine sediments. *Earth and Planetary Science Letters*, *64*(2), 213–230. https://doi.org/10.1016/0012-821x(83)90205-4
Sayles, F. L. (1979). The composition and diagenesis of interstitial solutions-I. Fluxes across the seawater-sediment interface in the Atlantic Ocean. *Geochimica et Cosmochimica Acta*, *43*(4), 527–545. https://doi.org/10.1016/0016-7037(79)90163-7
Schlesinger, W. H., Klein, E. M., & Vengosh, A. (2017). Global biogeochemical cycle of vanadium. *Proceedings of the National Academy of Sciences*, *114*(52), E11092. https://doi.org/10.1073/pnas.1715500114
Schlitzer, R. (2020). Ocean data view.
Scholz, F., Hensen, C., Noffke, A., Rohde, A., Liebetrau, V., & Wallmann, K. (2011). Early diagenesis of redox-sensitive trace metals in the Peru upwelling area—Response to ENSO-related oxygen fluctuations in the water column. *Geochimica et Cosmochimica Acta*, *75*(22), 7257–7276. https://doi.org/10.1016/j.gca.2011.08.007
Sclater, F. R., Boyle, E., & Edmond, J. M. (1976). On the marine geochemistry of nickel. *Earth and Planetary Science Letters*, *31*(1), 119–128. https://doi.org/10.1016/0012-821x(76)90103-5
Sharp, J. O., Lezama-Pacheco, J. S., Schofield, E. J., Junier, P., Ulrich, K.-U., Chinni, S., et al. (2011). Uranium speciation and stability after reductive immobilization in aquifer sediments. *Geochimica et Cosmochimica Acta*, *75*(21), 6497–6510. https://doi.org/10.1016/j.gca.2011.08.022
Shaw, T. J., Gieskes, J. M., & Jahnke, R. A. (1990). Early diagenesis in differing depositional environments: The response of transition metals in pore water. *Geochimica et Cosmochimica Acta*, *54*(5), 1233–1246. https://doi.org/10.1016/0016-7037(90)90149-f
Shiller, A. M., & Boyle, E. A. (1987). Dissolved vanadium in rivers and estuaries. *Earth and Planetary Science Letters*, *86*(2–4), 214–224. https://doi.org/10.1016/0012-821x(87)90222-6

Smedley, P. L., & Kinniburgh, D. G. (2017). Molybdenum in natural waters: A review of occurrence, distributions and controls. *Applied Geochemistry*, *84*, 387–432. https://doi.org/10.1016/j.apgeochem.2017.05.008

Smith, D. C., Simon, M., Alldredge, A. L., & Azam, F. (1992). Intense hydrolytic enzyme activity on marine aggregates and implications for rapid particle dissolution. *Nature*, *359*(6391), 139–142. https://doi.org/10.1038/359139a0

Smrzka, D., Zwicker, J., Bach, W., Feng, D., Himmler, T., Chen, D., & Peckmann, J. (2019). The behavior of trace elements in seawater, sedimentary pore water, and their incorporation into carbonate minerals: A review. *Facies*, *65*(4), 1–47. https://doi.org/10.1007/s10347-019-0581-4

Steiner, Z., Landing, W. M., Bohlin, M. S., Greaves, M., Prakash, S., Vinayachandran, P. N., & Achterberg, E. P. (2022a). Variability in the concentration of lithium in the Indo-Pacific Ocean. *Global Biogeochemical Cycles*, *36*(6), e2021GB007184. https://doi.org/10.1029/2021gb007184

Steiner, Z., Lazar, B., Erez, J., & Turchyn, A. V. (2018). Comparing Rhizon samplers and centrifugation for pore-water separation in studies of the marine carbonate system in sediments. *Limnology and Oceanography: Methods*, *16*(12), 828–839. https://doi.org/10.1002/lom3.10286

Steiner, Z., Lazar, B., Torfstein, A., & Erez, J. (2017). Testing the utility of geochemical proxies for paleoproductivity in oxic sedimentary marine settings of the Gulf of Aqaba, Red Sea. *Chemical Geology*, *473*, 40–49. https://doi.org/10.1016/j.chemgeo.2017.10.012

Steiner, Z., Rae, J. W. B., Berelson, W. M., Adkins, J. F., Hou, Y., Dong, S., et al. (2022b). Authigenic formation of clay minerals in the abyssal North Pacific. *Global Biogeochemical Cycles*, *36*(11), e2021GB007270. https://doi.org/10.1029/2021gb007270

Steiner, Z., Rae, J. W. B., Berelson, W. M., AdkinsHou, J. F. Y., Dong, S., Lampronti, G. I., et al. (2022c). Porewater and sediment data from the North Pacific CDisK-IV expedition. *PANGAEA*. https://doi.org/10.1594/PANGAEA.946881

Steiner, Z., Sarkar, A., Prakash, S., Vinayachandran, P. N., & Turchyn, A. V. (2020). Dissolved strontium, Sr/Ca ratios, and the abundance of Acantharia in the Indian and southern Oceans. *ACS Earth and Space Chemistry*, *4*(6), 802–811. https://doi.org/10.1021/acsearthspacechem.9b00281

Sullivan, K. A., & Aller, R. C. (1996). Diagenetic cycling of arsenic in Amazon shelf sediments. *Geochimica et Cosmochimica Acta*, *60*(9), 1465–1477. https://doi.org/10.1016/0016-7037(96)00040-3

Tagliabue, A. (2019). Elemental distribution: Overview. In J. K. Cochran, H. J. Bokuniewicz, & P. L. Yager (Eds.), *Encyclopedia of Ocean sciences* (3rd ed., pp. 122–127). Academic Press.

Takano, S., Tanimizu, M., Hirata, T., & Sohrin, Y. (2014). Isotopic constraints on biogeochemical cycling of copper in the ocean. *Nature Communications*, *5*(1), 5663. https://doi.org/10.1038/ncomms6663

Tribovillard, N., Algeo, T. J., Lyons, T., & Riboulleau, A. (2006). Trace metals as paleoredox and paleoproductivity proxies: An update. *Chemical Geology*, *232*(1–2), 12–32. https://doi.org/10.1016/j.chemgeo.2006.02.012

Twining, B. S., & Baines, S. B. (2013). The trace metal composition of marine phytoplankton. *Annual Review of Marine Science*, *5*(1), 191–215. https://doi.org/10.1146/annurev-marine-121211-172322

Twining, B. S., Baines, S. B., Vogt, S., & Nelson, D. M. (2012). Role of diatoms in nickel biogeochemistry in the ocean. *Global Biogeochemical Cycles*, *26*(4), GB4001. https://doi.org/10.1029/2011gb004233

Vance, D., Little, S. H., de Souza, G. F., Khatiwala, S., Lohan, M. C., & Middag, R. (2017). Silicon and zinc biogeochemical cycles coupled through the Southern Ocean. *Nature Geoscience*, *10*(3), 202–206. https://doi.org/10.1038/ngeo2890

Wehrli, B., & Stumm, W. (1989). Vanadyl in natural waters: Adsorption and hydrolysis promote oxygenation. *Geochimica et Cosmochimica Acta*, *53*(1), 69–77. https://doi.org/10.1016/0016-7037(89)90273-1

Wu, F., Owens, J. D., German, C. R., Mills, R. A., & Nielsen, S. G. (2022). Vanadium isotope fractionation during hydrothermal sedimentation: Implications for the vanadium cycle in the oceans. *Geochimica et Cosmochimica Acta*, *328*, 168–184. https://doi.org/10.1016/j.gca.2022.05.002

Wu, F., Owens, J. D., Scholz, F., Huang, L., Li, S., Riedinger, N., et al. (2020). Sedimentary vanadium isotope signatures in low oxygen marine conditions. *Geochimica et Cosmochimica Acta*, *284*, 134–155. https://doi.org/10.1016/j.gca.2020.06.013

Wurl, O., Shelley, R. U., Landing, W. M., & Cutter, G. A. (2015). Biogeochemistry of dissolved arsenic in the temperate to tropical North Atlantic Ocean. *Deep Sea Research Part II: Topical Studies in Oceanography*, *116*, 240–250. https://doi.org/10.1016/j.dsr2.2014.11.008

Zheng, L., Minami, T., Konagaya, W., Chan, C.-Y., Tsujisaka, M., Takano, S., et al. (2019). Distinct basin-scale-distributions of aluminum, manganese, cobalt, and lead in the North Pacific Ocean. *Geochimica et Cosmochimica Acta*, *254*, 102–121. https://doi.org/10.1016/j.gca.2019.03.038

Zheng, L., Minami, T., Takano, S., Ho, T.-Y., & Sohrin, Y. (2021). Sectional distribution patterns of Cd, Ni, Zn, and Cu in the North Pacific Ocean: Relationships to nutrients and importance of scavenging. *Global Biogeochemical Cycles*, *35*(7), e2020GB006558. https://doi.org/10.1029/2020gb006558

Zheng, L., Minami, T., Takano, S., & Sohrin, Y. (2022). Distributions of aluminum, manganese, cobalt, and lead in the western South Pacific: Interplay between the South and North Pacific. *Geochimica et Cosmochimica Acta*, *338*, 105–120. https://doi.org/10.1016/j.gca.2022.10.022